

## Water Resources Research

### RESEARCH ARTICLE

10.1029/2017WR021377

#### Key Points:

- Flow reattachment length over dunes can be predicted with one equation over a wide range of nonequilibrium conditions
- Transport stage and the magnitude of flow upwelling at a dune crest are used to understand the variety of dune shapes that exists
- In nonequilibrium conditions the spatial location and intensity of turbulence deviate considerably from previous research at equilibrium

#### Correspondence to:

C. A. Unsworth,  
christopher.unsworth@hull.ac.uk

#### Citation:




Unsworth, C. A., Parsons, D. R., Hardy, R. J., Reesink, A. J. H., Best, J. L., Ashworth, P. J., & Keevil, G. M. (2018). The impact of nonequilibrium flow on the structure of turbulence over river dunes. *Water Resources Research*, 54. <https://doi.org/10.1029/2017WR021377>

Received 27 JUN 2017

Accepted 3 AUG 2018

Accepted article online 24 AUG 2018

## The Impact of Nonequilibrium Flow on the Structure of Turbulence Over River Dunes

C. A. Unsworth<sup>1</sup> , D. R. Parsons<sup>1</sup> , R. J. Hardy<sup>2</sup> , A. J. H. Reesink<sup>1,3</sup> , J. L. Best<sup>4,5</sup> , P. J. Ashworth<sup>6</sup> , and G. M. Keevil<sup>7</sup>

<sup>1</sup>Department of Geography, Environment and Earth Sciences, Faculty of Science, University of Hull, Hull, UK, <sup>2</sup>Department of Geography, Durham University, Durham, UK, <sup>3</sup>Now at Lancing College, Lancing, UK, <sup>4</sup>Department of Geology, University of Illinois, Urbana, IL, USA, <sup>5</sup>Departments of Geography and Geographic Information Science, Mechanical Science and Engineering and Ven Te Chow Hydrosystems Laboratory, University of Illinois, Urbana, IL, USA, <sup>6</sup>Division of Geography and Geology, School of Environment and Technology, University of Brighton, Brighton, UK, <sup>7</sup>School of Earth and Environment, University of Leeds, Leeds, UK

**Abstract** Most past experimental investigations of flow over river dunes have focused on conditions that match semiempirical flow-depth scaling laws, yet such equilibrium conditions are of limited value because they rarely occur in natural channels. This paper quantifies the structure of mean and turbulent flow over fixed 2-D laboratory dunes across a range of nonequilibrium conditions within the dune flow regime. The flow field was quantified using 2-D particle imaging velocimetry for 12 conditions, including flows that are too deep, too shallow, too fast, or too slow for the size of the fixed dunes. The results demonstrate major departures in the patterns of the mean flow and structure of turbulence when compared to dunes formed under equilibrium flow conditions. The length of flow reattachment scales linearly with the ratio of mean depth-averaged streamwise velocity to shear velocity at the dune crest ( $\bar{U}_c/u_c^*$ ), which provides a new predictive measure for flow reattachment length. Depth-averaged vertical velocities at the dune crest ( $\bar{V}_c$ ) show a parabolic relationship with  $\bar{U}_c$ , peaking at  $\bar{U}_c \sim 0.60$  m/s, which matches the relationship of dune aspect ratio with transport stage present in mobile bed conditions. The spatial location of the turbulent wake was found to vary with flow depth and velocity, with lower  $\bar{U}_c$  and greater flow depths causing the wake to rise toward the free surface. Deeper flows are likely to show less flow convergence over the crests of dunes due to reduced interaction of turbulence with the free surface, resulting in a reduction of transport stage.

**Plain Language Summary** This piece of research expands our description of how rivers flow over dunes on a river bed. Most of the scientific communities' research to date has used unnaturally steady conditions to measure how water moves over dunes. Yet these flow conditions are not strictly true to the variety of conditions nature produces, most importantly during floods. This research is the first detailed description of a wide range of flow states over dunes and changes our present understanding of the structure of flow over dunes in rivers. Consequently, the scientific community will be able to use this new information to better model and simulate how rivers work, how they flood, and how they transport sediment toward the world's deltas.

### 1. Introduction

The structure of flow over dunes whose morphology is in equilibrium with flow has been researched extensively in laboratory experiments (Bennett & Best, 1995; Best, 2005a; Bradley & Venditti, 2017; Fedele & Garcia, 2001; Kadota & Nezu, 1999; Kwoil et al., 2016; Lefebvre et al., 2016; Maddux et al., 2003; Mazumder et al., 2009; McLean et al., 1999, 1994; Nelson et al., 1993; Nelson & Smith, 1989; Venditti, 2007) and simulated using Computational Fluid Dynamics (Chang & Constantinescu, 2013; Grigoriadis et al., 2009; Omidyeganeh & Piomelli, 2011, 2013a, 2013b; Omidyeganeh et al., 2013; Stoesser et al., 2008; Xie et al., 2014), which has led to general agreement concerning the nature of the flow field over idealized dune forms, as outlined in conceptual models of flow over dunes (Best, 2005b; Figure 1). However, natural rivers rarely attain a flow morphology equilibrium due to temporal and spatial variations in hydraulic geometry leading to flow decelerations and accelerations, as well as varying discharge on a range of timescales (Aberle et al., 2010; Amsler & Garcia, 1997; Chen et al., 2012; Prent & Hickin, 2001). Consequently, the *equilibrium* description of flow structure over dunes encapsulated in Figure 1 might apply to natural channels only in rare instances. Testing how

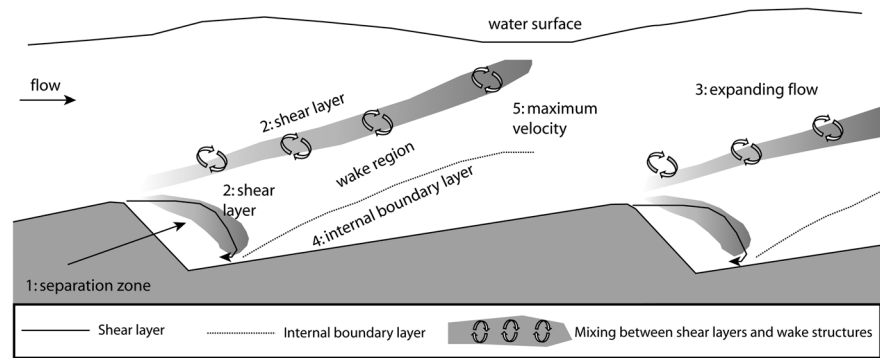


**Figure 1.** Conceptual diagram of steady unidirectional flow over equilibrium dunes. (1) Flow separation occurs in the lee of the dune, with reattachment approximately 4–6 dune heights downstream of the crest. (2) A shear layer is generated bounding the separation zone, with large-scale turbulence generated in the form of Kelvin-Helmholtz instabilities along this shear layer; as the free shear expands, it creates a wake zone that grows and dissipates downstream. (3) A region of expanding flow in the dune leeside. (4) Downstream of the region of flow reattachment, a new internal boundary layer grows as flow reestablishes itself and develops a more logarithmic velocity profile. (5) Maximum streamwise velocity occurs over the dune crest (figure adapted from Best, 2005b).

flow deviates from such idealized conceptualizations, therefore, needs a new understanding of flow structure over dunes that deviates from an equilibrium description and applies to a range of nonequilibrium conditions.

Floods can change bed shear stress and bedform type through a flood hydrograph from ripples to dunes to an upper stage plane bed and back again. Often such changes occur with a temporal lag between the flow and bed state (Allen, 1978; Martin & Jerolmack, 2013; Nelson et al., 2011; Paarlberg et al., 2010; Shimizu et al., 2009). Experiments on the ripple-dune transition (Bennett & Best, 1996; Fernandez et al., 2006; Frias & Abad, 2013; Schindler & Robert, 2005) showed that during the transition, the location and intensity of flow separation (Figure 1, point 2), the turbulent wake (Figure 1), and the height of the internal boundary layer (Figure 1, point 4) vary in their spatial location and intensity. Best and Kostaschuk (2002) and Kwoil et al. (2016, 2017) have also shown that reductions in the leeside slope angle lessen the intensity and temporal consistency of flow separation (Figure 1, point 2), while Bennett et al. (1998) and Naqshband et al. (2016) examined the transition of dunes to upper stage plane bed and demonstrated the collapse of the flow separation feedback. All these experiments indicate deviations from the equilibrium dune flow description (Figure 1) due to alteration of the bed morphology. Yet while the majority of nonequilibrium conditions in natural channels remain within the dune regime during passage of a flood wave (Amsler & Garcia, 1997; Jordan, 1965; Julien & Klassen, 1995; Nittrouer et al., 2008; Wilbers, 2004; Wilbers & Ten Brinke 2003), there is a paucity of research describing the mean flow and turbulence structure under nonequilibrium conditions across this regime.

Engel (1981) demonstrated that variations in bedform geometry control the structure of flow over dunes, such as shear layer height and reattachment length ( $R_x$ ), which is considered stationary for a fixed morphology (Kadota & Nezu, 1999). Balachandar et al. (2007) showed that reattachment length increased when flow depth ( $Y$ ) was lowered below the equilibrium flow depth, indicating that under nonequilibrium conditions flow separation and reattachment are dependent on both flow conditions and bedform shape. In addition, experiments such as those of Fernandez et al. (2006) and Kwoil et al. (2016, 2017) demonstrate that bedform geometry can change reattachment length even under consistent flow boundary conditions. This variety of causal mechanisms indicates a multiplicity of controls upon reattachment length. Yet as demonstrated nearly 40 years ago by Engel (1981), the length of flow separation is controlled primarily by the magnitude of topographic acceleration, the interaction with the free surface, and the dissipation rate of turbulence. Herein, we aim to unify these seemingly different causal mechanisms by measuring reattachment length under a range of nonequilibrium conditions in order to identify a singular predictive mechanism.

Suspension of sediment affects the dynamics of turbulent flow (Baas et al., 2011, 2016), channel-wide sediment transport rates, bar growth, and even channel pattern (Nicholas et al., 2013). The macroturbulent structures that are produced from the shear layer of dunes (Best, 2005a, 2005b; Grigoriadis et al., 2009; Omidyeganeh & Piomelli, 2011; Stoesser et al., 2008) are capable of suspending higher than average

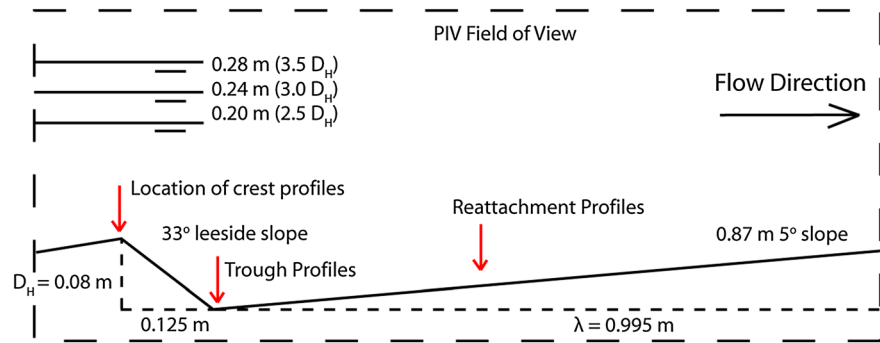


**Figure 2.** Scaled schematic diagram of laboratory dunes. The PIV field of view (large dashes) is centered over the middle dune. Mean bed level is 0.040 m. PIV = particle imaging velocimeter.

quantities of bed sediment (Kostaschuk & Church, 1993; Lapointe, 1992, 1996). Suspension of bed sediment has been put forward as a principal reason why dunes wash out (Bridge & Best, 1988; Carling, Williams, et al., 2000; Naqshband et al., 2016) at high transport stages  $>12 \theta^*/\theta_c^*$  (Lin & Venditti, 2013; Yalin, 1977), where  $\theta^*$  is the nondimensional Shields number and  $\theta_c^*$  is the critical Shields number for sediment motion. Bedforms at high transport stages reduce in height with increasing bed shear stress until the formation of upper stage plane beds (Bennett et al., 1998). Bedform shape does not remain constant across the dune regime, with short, steep dunes existing at low transport stages  $<8 \theta^*/\theta_c^*$  (Best, 1996; Carling et al., 2000), high-amplitude dunes around  $8\text{--}12 \theta^*/\theta_c^*$  (e.g., Bridge & Best, 1988), and washed out bedforms  $>12 \theta^*/\theta_c^*$  (e.g., Carling, Golz, et al., 2000; Saunderson & Lockett, 1983; Smith & Ettema, 1997). Such variation in bedform shape is not accounted for in published descriptions of turbulent flow structure over dunes, yet it is the intensity and spatial distribution of turbulence that is a primary control on the locations of erosion and deposition that defines dune shape (Bennett & Best, 1996; Nelson et al., 1995; Schmeckle, 2014).

In order to investigate the relationships highlighted above, the present paper examines measurements of the mean and turbulent structure of flow over fixed, idealized, 2-D dune shapes under nonequilibrium flow-morphology conditions. In the experiments detailed herein, the flow Reynolds number is changed systematically through variations in depth and mean velocity, so that the nonequilibrium flow conditions produced are too slow, too fast, too deep, and too shallow for the fixed bedform conceptual model of dune flow (Figure 1).

## 2. Methods

### 2.1. Flume Setup and Experimental Conditions

A 1-m wide, 1-m deep, and 10-m long recirculating flume was used to quantify the flow field over two-dimensional (straight crested) idealized dune forms. Three fixed 2-D dune forms of wavelength = 0.995 m were constructed marine plywood and fixed to the flume bed (Figure 2), with dune height being 0.08 m ( $= D_H$ ) in order to scale with bedform wavelength under scaling ratios reported in past research (Allen, 1982). The slope of the dune lee face was set at the angle of repose ( $\sim 33^\circ$ ) so that the steepness and lee slope angle were consistent with bedload-dominated dunes (Bennett & Best, 1995). Quartz sand of  $D_{50} = 0.5$  mm was glued to the bedform surface to provide an appropriate grain roughness.

The equilibrium depth of flow over dunes generated in laboratory experiments is usually reported as  $\sim 3 D_H$  (Allen, 1982; Bradley & Venditti, 2017; Guy et al., 1966; Yalin, 1964), and the present study investigated conditions both above and below this value. Naming conventions for experimental conditions here follow a structure of flow depth (*High* [280 mm], *Medium* [240 mm], *Low* [200 mm]) followed by mean velocity in centimeter per second. For example, the nearest condition to equilibrium flow was in run *M84* (Table 1), which has a medium depth of 240 mm ( $3.0 D_H$ ) and a mean velocity of 0.84 m/s. In all experiments, the flow was fully turbulent and subcritical (Table 1). Flow velocities were varied from 0.14 to 0.92 m/s for the deepest flows (e.g., H14 to H92) and from 0.18 to 0.75 m/s for the shallowest conditions (e.g., L18 to L75). Width-to-depth ratios of the flow were thus between 3.5 and 5 (Table 1), implying that wall-induced secondary circulation was not significant in the center of the channel (Williams, 1970).

**Table 1**  
Boundary Conditions of the Experimental Runs

Experimental run	Y (m)	$\bar{U}_c$ (m/s) crest	$\bar{V}_c$ (m/s) crest	Fr	Re	Q (m <sup>3</sup> /s)	$R_x/D_H$	Maximum Reynolds stress ( $\tau_R$ ) (n/m <sup>2</sup> )	Boundary shear stress ( $\tau_b$ ) (Reynolds extrapolation) (n/m <sup>2</sup> )		Shields $\theta^*$ and critical shields $\theta_c^*$	
									Spatially averaged $Z_0 = \text{MBL}$	Crest profile $Z_0 = \text{crest}$	$\theta^*$ (spatial average)	$\theta^*/\theta_c^*$
H14	0.28 (3.5 $D_H$ )	0.14	0.0002	0.08	39000	0.038	4.20	0.30	0.14	0.031	0.02	0.42
H30	0.28 (3.5 $D_H$ )	0.30	0.0081	0.18	83000	0.085	3.96	1.60	0.77	0.31	0.10	2.31
H61	0.28 (3.5 $D_H$ )	0.61	0.0155	0.37	170000	0.17	4.04	6.20	3.23	1.33	0.40	9.70
H76	0.28 (3.5 $D_H$ )	0.76	0.0108	0.46	213000	0.21	4.00	9.10	4.79	1.99	0.59	14.39
H92	0.28 (3.5 $D_H$ )	0.92	0.0077	0.56	258000	0.25	4.09	16.00	9.50	3.22	1.17	28.54
M14	0.24 (3 $D_H$ )	0.14	0.007	0.10	35000	0.035	4.09	0.28	0.18	0.080	0.02	0.54
M23	0.24 (3 $D_H$ )	0.23	0.0079	0.15	55000	0.055	4.31	1.00	0.50	0.19	0.06	1.50
M84	0.24 (3 $D_H$ )	0.84	0.0087	0.37	200000	0.20	4.40	11.50	6.70	2.03	0.83	20.13
L18	0.2 (2.5 $D_H$ )	0.18	0.007	0.13	37000	0.037	3.90	0.45	0.33	0.14	0.04	0.99
L42	0.2 (2.5 $D_H$ )	0.42	0.0106	0.30	85000	0.085	4.14	3.20	1.59	0.54	0.20	4.78
L62	0.2 (2.5 $D_H$ )	0.62	0.0124	0.44	124000	0.12	4.25	6.30	3.01	1.025	0.37	9.04
L75	0.2 (2.5 $D_H$ )	0.75	0.0099	0.53	147000	0.15	4.43	10.00	5.26	1.79	0.65	15.80

Two-dimensional (streamwise ( $u$ ) and vertical ( $v$ )) flow velocity fields were quantified for each experimental condition using a Dantec™ 100-Hz particle imaging velocimeter (PIV) (Adrian, 2005; Hardy et al., 2005). The laser was positioned so that the field of view was along the centerline of the flume and centered on the mid-stoss of the middle dune (Figure 2). This setup illuminated the flow field over the measurement dune across a horizontal distance of 1.004 m and to a height of 0.62 m. The field of view of the PIV analysis was less than the flow depth due to the necessity of masking the near surface flow in order to remove free surface reflections from the PIV analysis. The flow field was measured for 80 s/run, yielding an array of ~8,000, 2 megapixel images of the flow field. This 80-s measurement time was sufficient for the mean flow statistics to converge to a statistically steady state (Hardy et al., 2005; Rhoads et al., 2001) and thus was representative of the time-averaged flow conditions. Image quality was improved by removing the mean intensity image from the image set to remove constant reflections and glare. To improve the signal-to-noise ratio, images were sharpened using a  $3 \times 3$  high-pass filter, and following Adrian and Westerweel (2011) a signal-to-noise threshold of 7:1 was used to ensure that calculations in poorly seeded and/or illuminated areas did not occur. Flow vectors were calculated using an adaptive correlation algorithm (Theunissen et al., 2010) on a  $32 \times 32$  pixel grid with a 75% overlap. One initial step of  $64 \times 64$  pixel grid size was used to guide analysis, with no subpixel refinement or deforming windows being used. This produced output interrogation grid cells of  $32 \times 32$  pixels that were  $6.4 \text{ mm}^2$  across the field of view, yielding 157 cells horizontally and 51, 36, and 27 pixels vertically for the three depths 280 (H), 240 (M), and 200 mm (L), respectively. Postprocessing of the vector arrays was accomplished using a  $3 \times 3$  pixel median detection algorithm that locates and removes spurious vectors (Westerweel & Scarano, 2005), with vectors replaced with the median vector of the  $3 \times 3$  window. Vector removal and interpolation changed an average of 1% of the vectors across all the runs, with particles moving no more than 6 pixels per time step, which is less than the 8-pixel limit defined from the  $32 \times 32$  interrogation window and the one fourth rule (Adrian & Westerweel, 2011). Maximum particle displacement was less than 3.7% per interrogation window, and the accuracy of the measured velocities was determined to be  $\pm 0.001 \text{ m/s}$ .

## 2.2. Analysis of Turbulent Flow Statistics

Analysis of the 2-D flow field was performed using the conventional methods of calculating the time-averaged downstream ( $\bar{U}$ ) and vertical ( $\bar{V}$ ) velocities for each point. Quadrant analysis was performed on the time-varying flows following the methods of Lu and Willmarth (1973). Quadrant analysis involves partitioning the flow into four groups (or quadrants) dependent on the magnitude of variation in  $u$  and  $v$  from the time-averaged values at the same points, and above a user-set threshold. In the present study, a threshold value (whole size) of 1 standard deviation was used to capture a large proportion of the turbulent events

across all conditions (Bennett & Best, 1995). Traditional studies of uniform, canonical turbulent boundary layers over flat smooth surfaces possess a mean streamline vector that is parallel to the bed (Bogard & Tiederman, 1986; Lu & Willmarth, 1973). However, this parallel streamline assumption may not be appropriate in cases where the bed is sloping, such as in this case of flow over bedform stoss and lee slopes. To account for the varying streamline in full, and following Omidyeganeh and Piomelli (2013a, 2013b), the quadrant definitions are rotated to the depth-averaged mean streamline vector for each profile in each experiment. This rotation was performed to provide a quadrant analysis that is relevant to the mean flow conditions across each individual run. The largest rotation applied ( $\sim 3^\circ$ ) was in the flow separation zone and is significantly less than the slopes of the bedform. The rotation improves the identification of quadrant 2 and 4 events near the bed, which are key flow structures that are important in initiating and maintaining sediment motion (Best, 1992; Diplas et al., 2008; Grass, 1983; Nelson et al., 1995; Schmeckle, 2014; Schmeckle et al., 2007), and in suspending bed sediment (Garcia et al., 1996; Nino et al., 2003; Wren et al., 2007).

Bed shear stress ( $\tau_b$ ) was estimated using the method of Nelson et al. (1993) and Bennett and Best (1995), where the intercept (mean bed level) of the linear portion of the spatially averaged (from reattachment to crest) Reynolds stress profile provides a direct estimate of  $\tau_b$ . The Reynolds stress ( $\tau_R$ ) was calculated using the standard two-dimensional Reynolds decomposition:

$$\tau_R = -\rho \overline{uv} \quad (1)$$

$$-\overline{uv} = \frac{1}{n} \sum_{i=1}^n (u_i - \bar{U})(v_i - \bar{V}) \quad (2)$$

where  $\overline{uv}$  is the mean product of the fluctuating components of the downstream and vertical velocities.  $\bar{U}$  and  $\bar{V}$  are the time-averaged velocities,  $u_i$  and  $v_i$  are instantaneous velocities, and  $n$  is the number of observations.

The shear velocity was calculated using

$$u^* = (\tau_b/\rho)^{0.5} \quad (3)$$

where  $\rho$  is the fluid density (1,000 kg/m<sup>3</sup>). A nondimensional grain size ( $D_*$ ) was calculated using the method of Van Rijn (1984):

$$D_* = D_{50} \left[ \frac{(s-1)g}{\nu^2} \right]^{1/3} \quad (4)$$

where the grain size ( $D_{50}$ ) is 0.5 mm,  $s$  is the relative density of sand in water (1.65),  $g$  is acceleration due to gravity (9.81 m<sup>2</sup>/s), and  $\nu$  is the kinematic viscosity of water (1.004 × 10<sup>-6</sup> m<sup>2</sup>/s). Equation (4) produces a  $D_*$ -value of 6.41. The Shields number ( $\theta^*$ ) and critical Shields number ( $\theta_c^*$ ) for the sediment were estimated using the method of Soulsby (1997):

$$\theta^* = \frac{\tau_b}{sgD_{50}} \quad (5)$$

$$\theta_c^* = 0.3/(1 + 1.2D_*) \times 0.055 * (1 - e^{(-0.02 * D_*)}) \quad (6)$$

and yielded a critical Shields number of 0.041.  $\theta^*/\theta_c^*$  values for each condition (Table 1) show that the sediment transport stage varied from 0.4 to 28 across the experiments, therefore encompassing and exceeding the range of possible dune forming states (van den Berg & Van Gelder, 1993).

### 3. Results

#### 3.1. Mean Flow Velocities

To describe the wide range of flow conditions simply but systematically, the following text refers to *fast* and *slow* conditions in addition to the experimental name. To delineate between fast and slow conditions in an objective manner, we found that the amount of flow upwelling at the crest provided a suitable process to allow such differentiation. The depth-averaged mean vertical velocity at the crest ( $\bar{V}_c$ ) changes

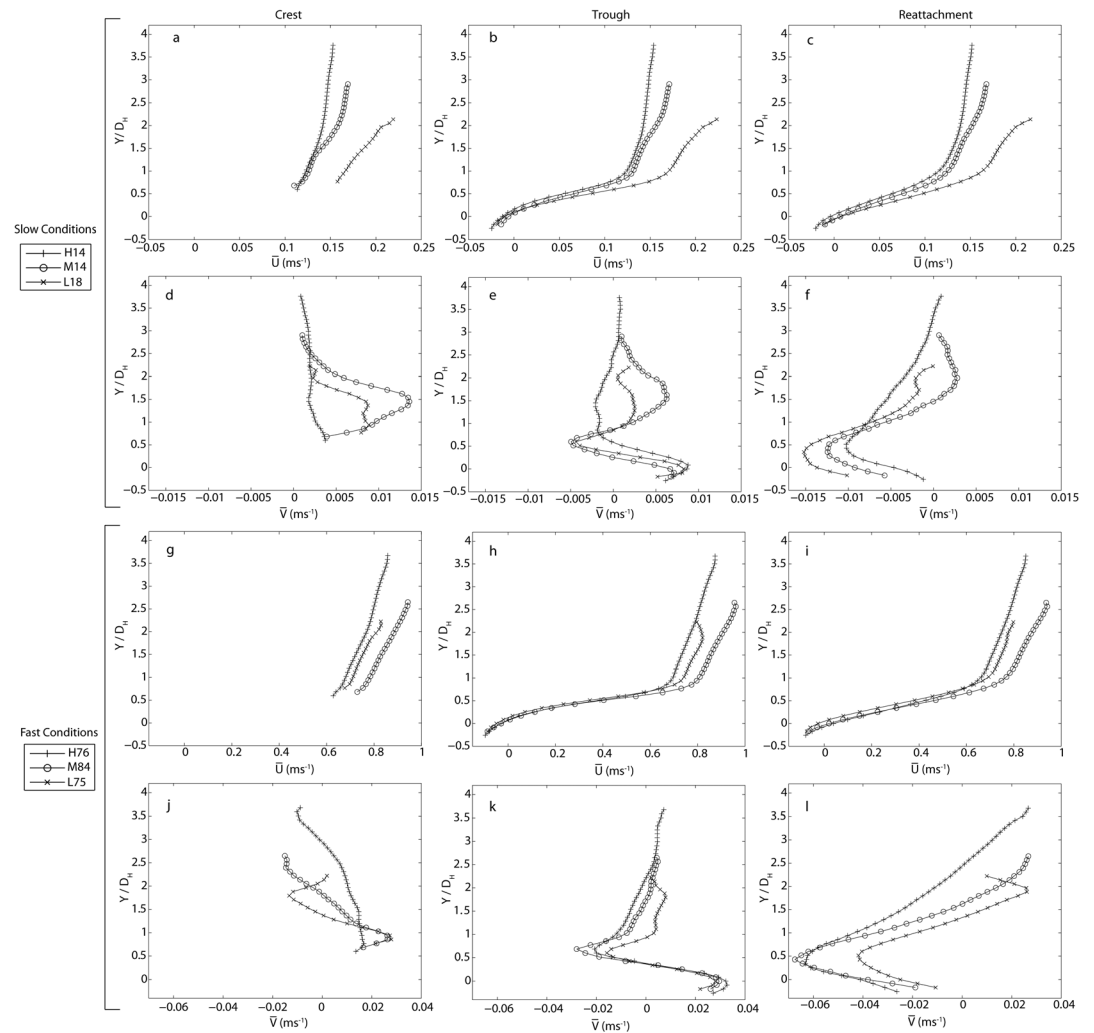


**Figure 3.** Time-averaged velocity profiles of streamwise velocity,  $\bar{U}$  (a–c for comparably slow flow conditions, g–i for comparably fast flow conditions) and vertical velocity,  $\bar{V}$  (d–f for slow flow conditions and j–l for fast flow conditions). Left column = profiles at crest; middle column = profiles at trough; right column = profiles at near reattachment. Ordinate axis = normalized profile height where 0.5 = the dune crest, 0 = mean bed level. Abscissa axis is the velocity magnitude in meter per second. The figure shows variations in shape of the velocity profile with changes in flow depth with comparable depth-averaged streamwise velocities.

parabolically with the depth-averaged mean downstream velocity at the dune crest ( $\bar{U}_c$ ) (Table 1), with the highest  $\bar{V}_c$  occurring at  $\sim 0.60$  m/s  $\bar{U}_c$  for all depths (Table 1) at  $\sim 9 \theta^*/\theta_c^*$ . Also notable is the near-zero  $\bar{V}_c$  for condition H14, a condition that has a  $\theta^*/\theta_c^*$  of less than unity. Conditions with a  $\bar{U}_c > 0.60$  m/s are herein referred to as fast conditions, whereas conditions with  $\bar{U}_c < 0.60$  m/s are referred to as slow conditions, based upon the peak upwelling velocity at the crest ( $\bar{V}_c$ ) at the crest across all depths and the peak in dune aspect ratio found in previous research using mobile bed conditions  $\sim 9 \theta^*/\theta_c^*$  (Vendetti et al., 2016; Yalin, 1977).

Profiles of  $\bar{U}_c$  and  $\bar{V}_c$  (Figure 3) across all depths ( $Y$ ) for the most comparable slowest (H14, M14, and L18) and fastest (H76, M84, and L75)  $\bar{U}_c$  conditions show that the absolute shape of the  $\bar{U}_c$  profile changes considerably with variation in  $Y$ . Condition H14 has the lowest gradient in  $\bar{U}_c$  above  $1 D_H$  above the crest and maintains an approximate log-linear profile shape. Condition M14 displays an increase in mean velocity above  $1.5 D_H$  (Figure 3a), while condition L18 has a single gradient velocity profile. The changes in profiles of  $\bar{V}_c$  at comparable  $\bar{U}_c$  conditions with different  $Y$  (Figure 3d) show four important features: (1) at all depths and at low  $\bar{U}_c$

conditions, the vertical velocity at the crest is always positive (i.e., upward away from the bed); (2) for H14, there is very little gradient in the vertical velocity; (3) the equilibrium depth profile (M14) has both the highest gradient and highest magnitude in vertical velocity, and (4) at the lowest depth condition (L18), similar patterns in vertical velocity are present but with smaller overall velocity magnitudes than for the equilibrium depth (M14) condition.

At faster  $\bar{U}_c$  conditions across all depths (Figures 3g and 3j), the vertical velocity at the crest becomes negative at different elevations above the crest for each condition. The switch from positive to negative vertical velocities occurs at a higher relative location in the profile at greater  $Y$ . The direction of the vertical velocity for the low  $Y$  condition (L75) switches at  $1 D_H$  above mean bed level; for the medium  $Y$  condition (M84), the switch from positive to negative occurs at  $1.5 D_H$  above mean bed level, whereas for the high  $Y$  condition (H76) this occurs at  $3 D_H$ 's. The increase in  $\bar{U}_c$  from 0.14 to 0.75 m/s (Figures 3a and 3d and Figures 3g and 3j) also produced changes in the mean downstream velocity profile at the crest. The shape of the velocity profile for M84 (the nearest to equilibrium) changes from a log-linear profile at the lower  $\bar{U}_c$  condition (M14, Figure 3a) to a single, higher, gradient profile at M84 (Figure 3g). This change in shape with higher  $\bar{U}_c$  is also seen at the lower depth condition ( $2.5 D_H$ ). The free stream (lognormal) flow pattern seen in the upper half of the profiles in Figure 3a is much less clear at higher  $\bar{U}_c$  as well as at lower  $Y$  conditions. However, the highest  $Y$  run in Figure 3a maintains its log-linear profile shape even at the higher  $\bar{U}_c$  condition.

Figures 3b and 3e show the mean downstream and vertical velocity profiles in the dune trough for the slow velocity conditions (H14, M14, and L18). The shear layer produced by flow separation at the dune crest can be seen as a distinct kink in all the profiles of downstream and vertical velocity at  $\sim 0.7 D_H$ . At all  $Y$ , there is consistency in the shape of the mean downstream and vertical profiles through the recirculating flow and shear layer. Above the shear layer, the profiles diverge toward the free surface in a similar pattern to that at the crest (Figures 3a and 3g) but with some key differences. For condition H14, the vertical velocity in the trough (Figure 3e) above the shear layer ( $>0.7 D_H$ ) is negative for a substantial portion of the profile, whereas for the shallower condition, M14, the vertical velocity in the same section is positive (Figure 3b). This outcome is maintained at larger  $\bar{U}_c$  conditions (Figure 3k). The sequential reductions in depth from conditions H76 to M84 and L75 also alter the location of the change from negative to positive vertical velocity, which occurs at  $1, 2,$  and  $2.5 D_H$  above the mean bed level for H76, M84, and L75, respectively (Figure 3k).

The locations of the profiles of mean velocity shown in Figures 3c, 3f, 3i, and 3l are slightly upstream of the median reattachment point (defined below), plotted to illustrate the changes in the location and magnitude of flow recirculation near reattachment for all flow conditions. Figures 3c and 3f plot the mean downstream and vertical velocity profiles for the slowest flow conditions, H14, M14, and L18, while Figures 3i and 3l depict these profiles for the fast flow conditions (H76, M84, and L75). For all sets of  $\bar{U}_c$  and  $Y$  (Figures 3c, 3f, 3i, and 3l), the mean downstream velocity is negative  $\sim 0.5 D_H$  above the mean bed level, with the downstream point at which downwelling starts varying between  $1$  and  $3.5 D_H$  above the mean bed level. The direction of vertical flow near the bed at reattachment is strongly negative across all variations in  $Y$  (Figures 3f and 3l), with the vertical velocity near the bed at the lower  $\bar{U}_c$  conditions (Figure 3f) having a consistent pattern of increasingly negative values at lower  $Y$ . A reverse pattern occurs at faster  $\bar{U}_c$  conditions (H76, M84, and L75, Figure 3l), yet despite this, the shear layer height remains the same as the height of the crest ( $0.5 D_H$  above the mean bed level) across all  $\bar{U}_c$  and  $Y$ . However, the difference in vertical location ( $Y/D_H$ ) where upwelling and downwelling occur is controlled by a combination of  $\bar{U}_c$  and  $Y$ . For upwelling of flow at reattachment, Figure 3f shows that an increase in  $\bar{U}_c$  has, at each  $Y$ , substantially altered the location above the shear layer ( $>0.5 D_H$ ) where the flow begins to upwell (Figures 3f and 3l), with mean upwelling flow existing  $\sim 0.5$  to  $1 D_H$  closer to the bed at the higher  $\bar{U}_c$  conditions across the three flow depths.

### 3.2. Reattachment Length

Table 1 shows the calculated reattachment length ( $R_x$ ) for all runs using the median method of 50% negative flow velocities to define the location of flow reattachment at the bed (Kadota & Nezu, 1999; Simpson, 1996). The median reattachment length ( $R_x$ ) across all conditions is  $4.15 D_H$  downstream of the crest (Table 1), and the flow velocity only affects reattachment length for the low flow depth conditions (L18 to L75). This change in reattachment length coincides with the higher gradient in the mean downstream velocity profile at the

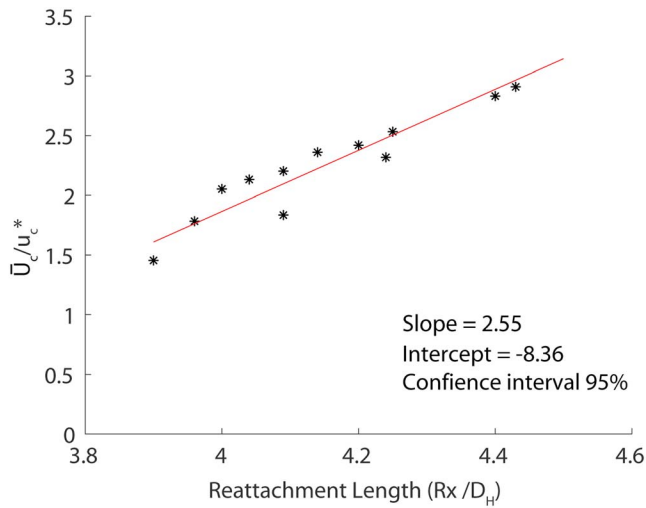


**Figure 4.** Length of reattachment of the flow separation zone ( $R_x$ ) normalized by the dune height ( $D_H$ ) plotted against depth-averaged downstream velocity at the crest ( $\bar{U}_c$ ) normalized by the shear velocity calculated using the law of the wall at the crest ( $u_c^*$ ). The line of best fit is the geometric mean regression at a confidence interval of 95%. Indicating a strong linear relationship between  $\bar{U}_c/u_c^*$  and reattachment length.

crest in the low  $Y$  conditions (Figure 3g), as compared to the log-linear velocity profile shape present at the higher  $Y$  conditions (e.g., H14 with H76). Although the height of flow reversal near flow reattachment did not change with variations in  $Y$  or  $\bar{U}_c$  (Figures 3b and 3h),  $R_x$  does increase with  $\bar{U}_c$  for the low  $Y$  conditions (Figure 4). Condition M84 has a very similar  $R_x$  to that in L75, which has a similar  $\bar{U}_c$ , and shape of the  $\bar{U}$  profile at the crest (Figure 3g). Therefore, a measure of flow magnitude and the shape of velocity profiles may better describe the behavior of the reattachment length. Here the shear velocity ( $u^*$ ), as estimated using the law of the wall fitted to the entire mean downstream velocity profile at the crest, implicitly incorporates the gradient of downstream velocity. As such,  $\bar{U}_c/u_c^*$  should provide a reasonable measure of flow reattachment length. Figure 4 plots the geometric mean regression between  $\bar{U}_c/u_c^*$  and  $R_x/D_H$  at a confidence interval of 95%. This plot shows the normalized reattachment lengths scale linearly with  $\bar{U}_c/u_c^*$  ( $R_x/D_H = 2.25 \bar{U}_c/u_c^* - 8.36$ ), and that, across all depths and velocities measured herein, it is the shape of the velocity profile and velocity magnitude that sets the median reattachment length.

### 3.3. Quadrant Analysis

Quadrant 2 and 4 events have been shown to dominate sand bed sediment transport (Celik et al., 2013; Diplas et al., 2008; Schmeckle, 2014; Schmeckle et al., 2007; Wren et al., 2007) and are displayed in Figures 5

and 6, respectively, for the high  $Y$  conditions (Figures 5a–5e and 6a–6e), the equilibrium  $Y$  conditions (Figures 5f and 6g, and 6f and 6g), and the low  $Y$  conditions (Figures 5h–5k and 6h–6k). The most obvious feature across all conditions (Figures 5 and 6) is the shear layer downstream of the dune crest (indicated for the nearest to equilibrium condition M84), which is spatially consistent across the runs, with a more intense shear layer present at higher  $\bar{U}_c$  across all variations in  $Y$ . The downstream wake, and a stacked wake that is produced from the upstream dune that is advected downstream over and above the study dune (identified in Figures 5g and 6g), is located at  $\sim 1.5 D_H$  above the dune crest. This wake structure shows a considerable change in its percentage contributions with alterations in both  $Y$  and  $\bar{U}_c$ , while the shear layer remains spatially stable. The wake consists of Q2 and Q4 events with a temporal occurrence of  $\sim 12\text{--}14\%$ , while the stacked wake is dominated by Q2 events at  $\sim 12\text{--}14\%$  and  $\sim 6\text{--}8\%$  for Q4.

Figures 5a, 5f, and 5h and 6a, 6f, and 6h demonstrate several key changes in the structure of the wake along the dune stoss due to a reduction in  $Y$ . The wake (identified via Q2 and Q4 events) moves toward the bed along the stoss side of the dune, with the stacked wake from the upstream dune that advects over the study dune being largely absent for H14 (Figures 5a and 6). The stacked wake is more intense (6% to 12%) and spatially larger at lower depths (L18). Furthermore, both Q2 and Q4 show that for L18, the upstream wake is closer to the crest, while the shear layer in the field of view has the highest percentage contributions of Q2 and Q4 at a lower depth (L18).

The intensity and spatial extent of the percentage contribution of Q2 and Q4 events in the wake and stacked wake change considerably with velocity conditions at a constant  $Y$  (Figures 5a–5e, and 6a–6e). The condition shown in Figure 5a produced the maximum percentage of Q2 events in the wake zone but produced no noticeable upstream stacked wake. Increasing  $\bar{U}_c$  to 0.30 m/s (Figure 5b) produced a large and intense stacked wake over the dune in the field of view that is dominated by Q2 events with an 11–12% contribution. The stacked wake, as revealed by Q2 events in Figure 5, merges with the wake produced in the field of view at around  $8 D_H$  downstream of the crest (Figure 5b). This merger significantly influences the distribution of Q4 events at the bed, with an increase in both the intensity and elevation of Q4 events at around  $8\text{--}9 D_H$  downstream. Further increases in  $\bar{U}_c$  (H62 to H92, Figures 5c to 5e) produce smaller stacked wakes of reduced (12% to 9%) Q2 intensity over the dune lee and stoss slope, but with similar intensity at the crest (13%). Peak intensity (12–14%) Q2 and Q4 events reduce along the stoss slope ( $6\text{--}12 D_H$ ) with higher  $\bar{U}_c$  from H61 to H92 (Figures 5 and 6) and become focused toward reattachment. Q4 intensity along the upper stoss slope at  $\sim 8\text{--}12 D_H$  reduces from  $\sim 11\%$  to 9% for the same conditions, while Q2 intensity remains comparatively



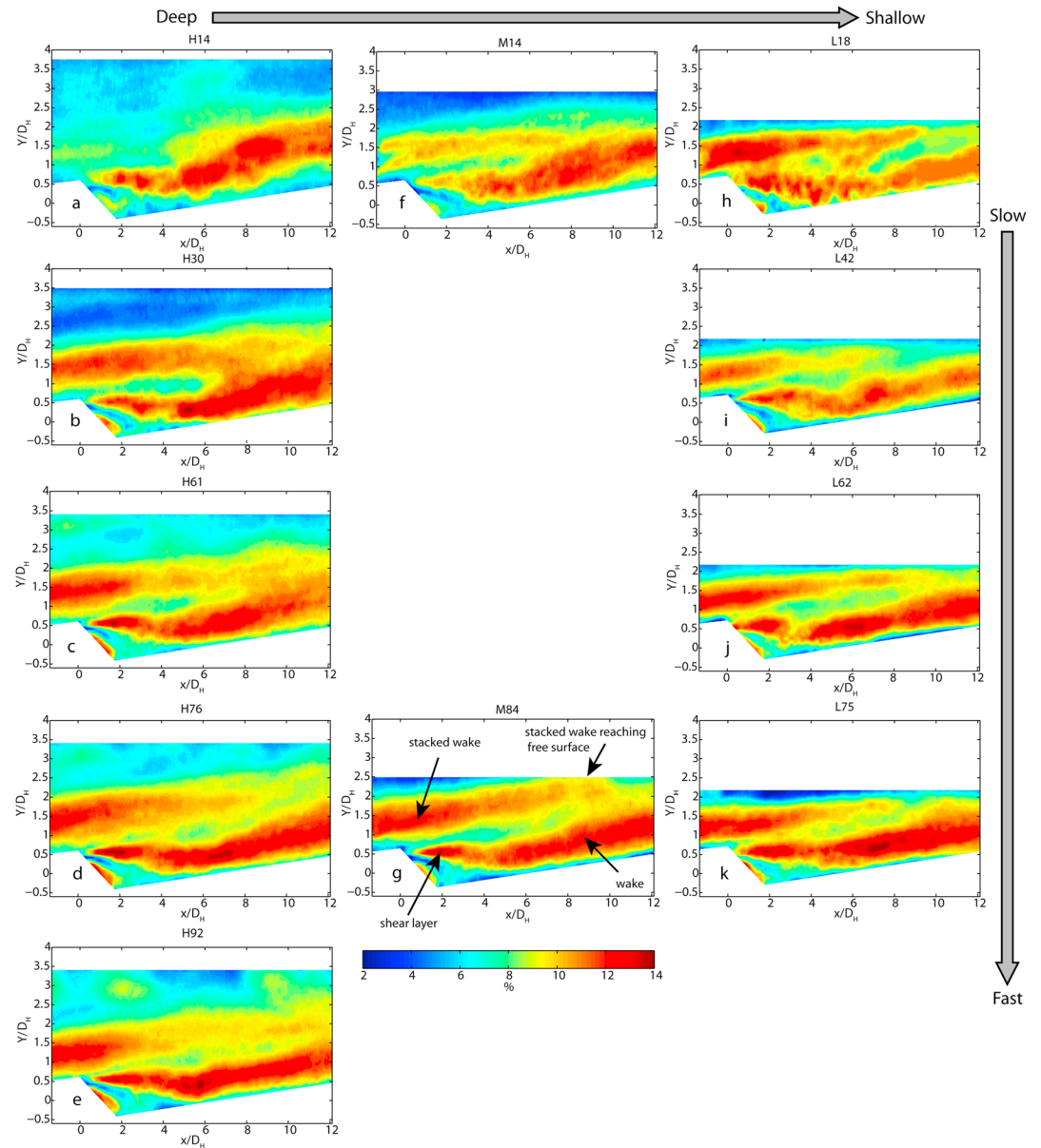


**Figure 5.** Plots of significant quadrant 2 ( $H > 1$ ) event contributions (color axis %).  $H = 0.28$ -m mean flow depth,  $M = 0.24$ -m mean flow depth,  $L = 0.2$ -m mean flow depth. The number after the depth =  $\bar{U}_c$  is in centimeter per second, for example, M84 = 0.24-m depth and 0.84 m/s.

constant. The percentage contribution of significant ( $H > 1$ ) Q2 events in the shear layer, and at the reattachment region, increases with higher  $\bar{U}_c$  (Figures 5c to 5e). Increasing  $\bar{U}_c$  also results in the stacked wake becoming more spatially confined, with events  $>12\%$  reducing from  $\sim 8 D_H$  downstream of the crest (Figures 5c and 5e) compared to  $4 D_H$  (Figure 5b). The vertical distance between the stacked wake and the dune crest and shear layer reduces with increasing  $\bar{U}_c$ , and similarly, the location of the peak in Q2 intensity along the stoss side moves upstream from  $\sim 8\text{--}10 D_H$  (Figure 5b) to  $6\text{--}8 D_H$  (Figure 5e), a position just downstream of reattachment.

The spatial distribution of Q4 events displays a similar pattern to that described for Q2 events. The higher intensity Q4 areas in the wake move toward the bed with increasing  $\bar{U}_c$  for all cases, but the change in the distribution of high percentage Q4 events with different  $\bar{U}_c$  is more complex. At high  $Y$ , there is an initial increase in Q4 events in the stacked wake with higher  $\bar{U}_c$  (Figures 6a–6c, 6% to 9%). Thereafter, and similar

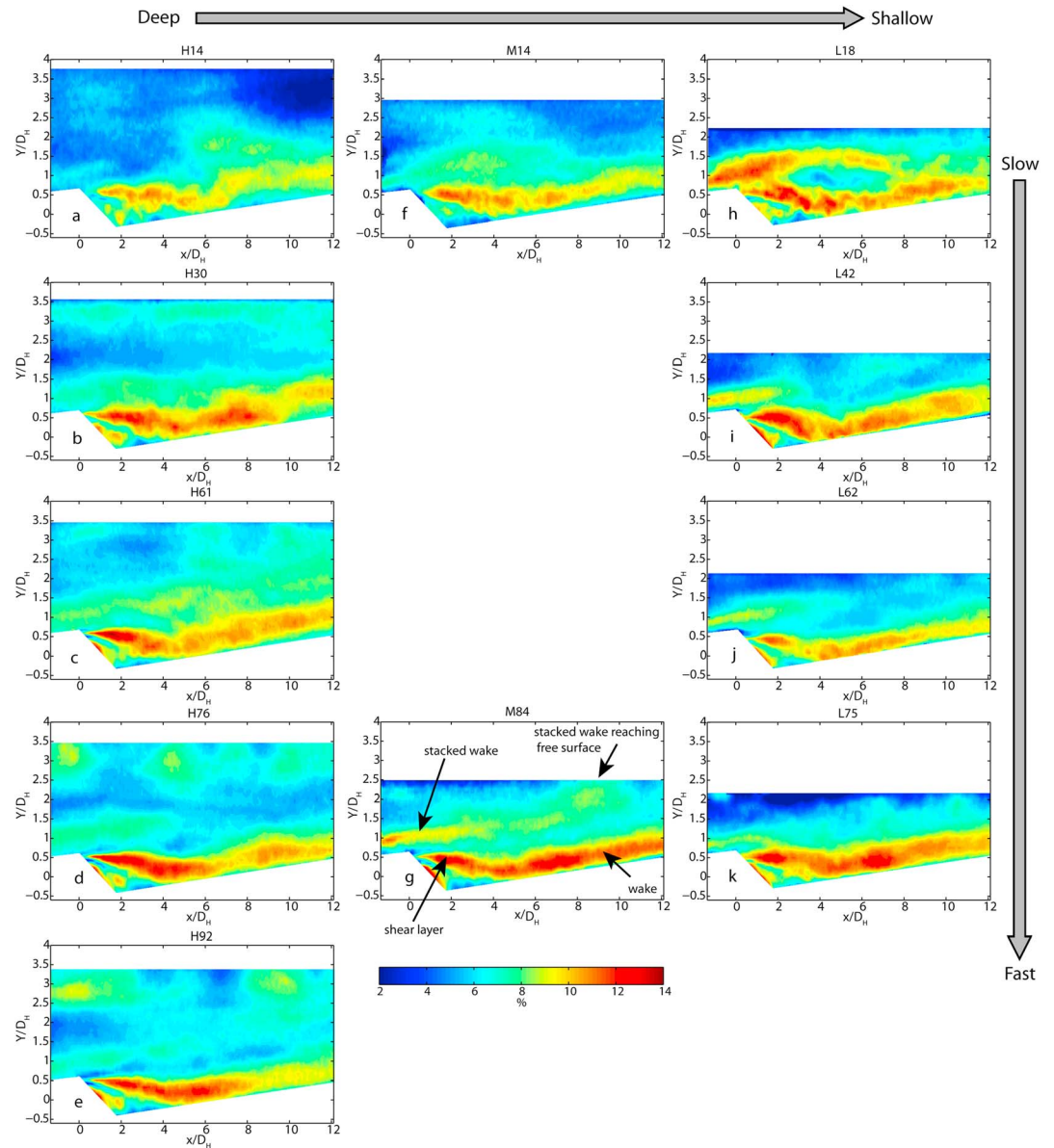


**Figure 6.** Plots of significant quadrant 4 ( $H > 1$ ) event contributions (color axis %).  $H = 0.28$ -m mean flow depth,  $M = 0.24$ -m mean flow depth,  $L = 0.2$ -m mean flow depth. The number after the depth =  $\bar{U}_c$  is in centimeter per second, for example, M84 = 0.24-m depth and 0.84 m/s.

to Q2, the percentage of Q4 events in the stacked wake above the crest reduces with at higher  $\bar{U}_c$  (Figures 5c to 5e, 9% to 6%). In Figures 5a and 6a, the wake produced by the study dune rises above the bed. In Figures 5b and 6b, the spatial distribution of Q4 events over the stoss slope is closer to the bed and of greater intensity (9% to 12% at  $8 D_H$ ). In Figure 6c, the stoss side exhibits an evenly distributed Q4 event intensity, but further increases in  $\bar{U}_c$  change the distribution and intensity of Q4 events again. The peak in the percentage of Q4 events migrates toward reattachment (8 to  $4 D_H$  from H30 to H92) and produces greater intensity of Q4 events near reattachment with higher  $\bar{U}_c$ .

Increasing  $\bar{U}_c$  at low  $Y$  conditions (Figures 5h to 5k) influences the distribution of Q2 events in different ways than for the higher  $Y$  conditions. Increasing  $\bar{U}_c$  at this lower depth results in an increase in the intensity and size of the wake produced in the field of view, while the intensity of the stacked wake reduces. This is also shown in the Q4 events (Figures 6h to 6k), with the percentage contributions in the stacked wake being

~11% (Figure 6h) but reducing to 9% (Figure 6k). In Figure 6h, the turbulent wake is close to the bed along the dune stoss, unlike at the higher depth in Figure 6a, and increases in intensity with increasing  $\bar{U}_c$  for both Q2 and Q4 (Figures 5h–5k and 6h–6k). A reduced  $Y$  also affects how the turbulent wake responds to higher  $\bar{U}_c$  conditions. For instance, at the high  $Y$  conditions (Figures 5 and 6a–6e), increasing  $\bar{U}_c$  induced a greater percentage of Q2 and especially Q4 events closer to the zone of reattachment, but for lower  $Y$  conditions the opposite pattern emerges, with the high percentage of Q2 events migrating downstream from around  $6 D_H$  to  $7$ – $9 D_H$  (Figures 5i to 5k) and  $\sim 8 D_H$  for Q4 events (Figures 6i–6k).

The intensity and position where turbulence reached the free surface also changed considerably with variations in  $\bar{U}_c$  and  $Y$ . At the deep and slow condition H14 (Figures 5a and 6a), Q2 and Q4 event contributions near the surface are ~2% to 6%. The spatial distribution of Q2 and Q4 near the free surface for the higher  $\bar{U}_c$  conditions H30 to H92 (Figures 5b–5e and 6b–6e) is all similar, with patches of Q2 and Q4 ~8% located above the crest, reattachment, and upper stoss slope. The maximum Q2 and Q4 event contributions near the free surface for the high  $Y$  conditions are in condition H92 (Figures 5e and 6e) at a value of 9%. The low  $Y$  conditions produced comparatively greater changes in intensity and spatial distribution of Q2 and Q4 events near the free surface compared with the high  $Y$  conditions. The stacked wake in the shallow and slow condition L18 (Figures 5h and 6h) has the highest contribution of any of the conditions measured here at ~12%. Increasing  $\bar{U}_c$  at this low  $Y$  in conditions L42 to L75 (Figures 5i–5k and 6i–6k) actually reduced the intensity of Q2 and Q4 events near the free surface by ~2–3%. The closest to equilibrium model condition, M84 (Figures 5g and 6g), produced Q2 and Q4 events >10% and >8%, respectively, at around  $10 D_H$  downstream of the crest near the free surface.

For all conditions tested, when the intensity of the turbulence in the wake increased, the stacked wake displayed a reduction in intensity; this indicates that turbulence production and dissipation occur more rapidly in the shear layer, with greater shear layer intensity at higher  $Y$  or lower  $\bar{U}_c$ . This wake interaction increased the intensity of significant turbulent events in both the shear layer and at reattachment (Figures 5 and 6a–6e). Moreover, the confinement of high Q2 and Q4 event intensities toward the reattachment region occurs alongside a change in Q2 and Q4 intensity in the stacked wake. At high  $Y$  conditions (Figures 5 and 6a–6e), the interaction between the stacked wake and shear layer moves the distribution of highest Q2 and Q4 events along the stoss slope toward reattachment, while at low  $Y$  the opposite change is observed—with the high percentage Q2 and Q4 events moving downstream with higher  $\bar{U}_c$  (Figures 5 and 6h–6k).

## 4. Discussion

### 4.1. Synthesis of Results

The laboratory results presented herein quantify the structure of the mean flow and turbulence over a fixed dune bed measured under nonequilibrium flow states, in order to observe how the flow structure changes with variations in relative submergence ( $Y/D_H$ ) and mean flow velocity. Figure 7 summarizes the variation in turbulent flow structure due to varying  $\bar{U}_c$  and  $Y$  for conditions H14, L18, H76, and L75. Several key points arise from the variations in flow structure revealed by these experiments.

1. Flow reattachment length ( $R_x$ ) did not change for flows that were deeper than equilibrium flow-morphology conditions (Table 1), and reattachment length can be given by the relationship  $R_x/D_H = 2.25 \bar{U}_c/u_c^* - 8.36$  (at the 95% confidence interval) when velocity at the crest is normalized by the shear velocity calculated from the same velocity profile.
2. The stacked wake produced from the upstream dune interacts with the shear layer and wake produced over the downstream dune, which increases the percentage of Q2 and Q4 events in the shear layer and wake zone relative to the wake produced over the downstream dune. This relationship is strongest under the lowest relative submergence and largest flow velocities measured.
3. The flow field downstream of flow reattachment changes substantially with mean flow velocity and flow depth. Depth and velocity have different effects. With greater mean downstream velocity at high flow depths, the topographic acceleration of flow over the stoss slope and wake stacking increased. In this shifting flow pattern, the location of the most frequent turbulent events along the stoss slope and the highest percentage Q2 and Q4 events migrated toward the reattachment zone. However, the greater mean downstream velocity at the lower flow depths produced the opposite trend.

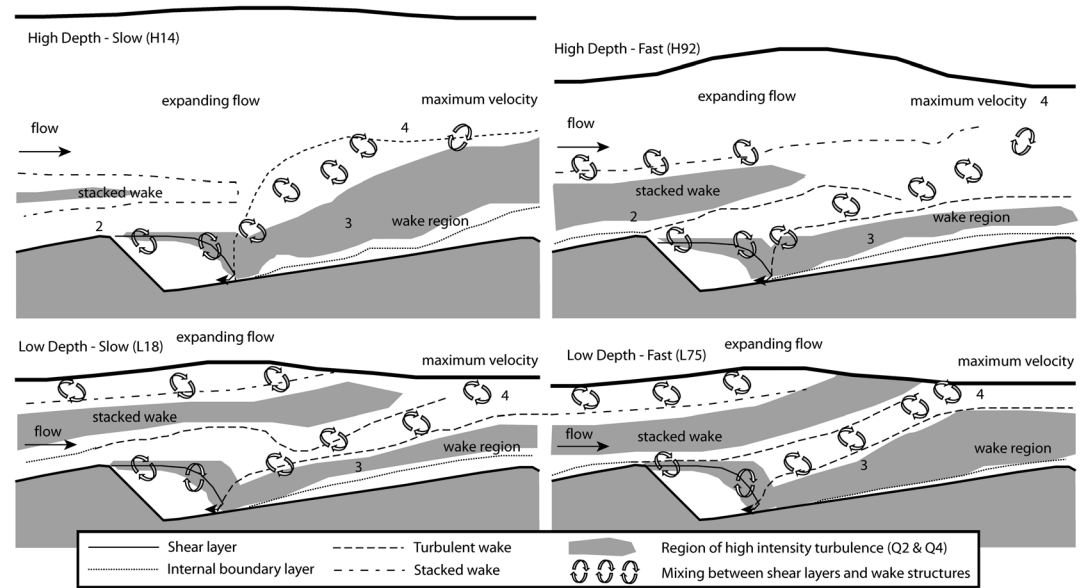


**Figure 7.** Summary conceptual diagram of turbulent flow over dunes in transient conditions using the deepest shallowest, fastest, and slowest conditions measured to illustrate the changes in spatial structure of turbulent dissipation and production.

4. The position along the dune where turbulence reached the free surface changed considerably, with greater mean velocities moving free surface interactions downstream of the dune crest (Figure 7). While lower flow depths produced greater percentages of Q2 events near the free surface, the location of high Q2 percentage events from the wake of the dune moved downstream, with the stacked wake interacting with the flow surface in the field of view. This change is due to the varying spatial extent of the stacked wake and topographic acceleration produced over the dune. In some instances, where mean flow velocity was low and the flow depth was high, turbulence generated by the shear layer and wake did not reach the free surface.

#### 4.2. Velocity Profiles

It is clear that flow depth plays a dominant role in defining the flow structure and shape of velocity profiles for the conditions measured herein. Even at low  $\bar{U}_c$ , there are significant changes to the shape of the downstream flow velocity profile across the three depth conditions measured (Table 1 and Figure 3). The mean downstream ( $\bar{U}_c$ ) profiles at the crest overlap near the bed but diverge at  $\sim 1.5 D_H$  above mean bed level (Figure 3a), which is indicative of two main flow features: (1) in less deep flows, the linear (form roughness) portion of the velocity profile remains consistent in height, and consequently, (2) the free flow above adjusts to a higher velocity to compensate for the reduction in  $Y$ . As the low flow depth conditions produce a single high gradient in the downstream velocity profile, the vertical distribution of form roughness and skin friction, usually partitioned in lognormal velocity profile shapes, becomes obscured, consequently limiting the applicability of law-of-the-wall estimates of bed shear stress at the dune crests (McLean et al., 1999) for these high relative roughness flow conditions. The differences in the mean vertical velocity at the crest ( $\bar{V}_c$ ) provide an indication of the scale of relative change in the location and intensity of the mean flow structures with higher  $\bar{U}_c$ .

The results also demonstrate how bedform shape strongly controls the mean velocity profiles in the recirculation region, with a constant shear layer height, as well as a constant reattachment length across the range of incoming flow velocities at high flow depths (Figure 4). However, when the mean downstream velocity profiles display a single gradient, as in experiment M84 and the low  $Y$  conditions, the length of the shear layer adjusts with  $\bar{U}_c$  (Figure 4). This indicates that a threshold in the behavior and response of the shear layer exists between the medium and low  $Y$  conditions. A key finding across the wide range of conditions tested is that a

threshold for such a change in flow structure over dunes exists close to the typical equilibrium depth and profile shapes seen at the flow-morphology equilibrium (Best, 2005b).

Engel (1981) found that for steep dunes, the length of flow separation did not change, as form drag was dominant, while altering dune morphology to low steepness dunes (Allen, 1968; Carling, Golz, et al., 2000; Saunderson & Lockett, 1983), otherwise known as *washed-out dunes* or *humpback dunes*, increases the relative significance of grain roughness compared to form drag, resulting in an increase in  $R_x$ . Importantly for the present study, the mean downstream velocity at low and high  $\bar{U}_c$  (Figures 3a and 3g) demonstrates that a reduction in  $Y$  causes the shape of the velocity profile at the dune crest to change from a log-linear profile at the higher flow depth to a single, linear profile for the low  $Y$  cases (Figure 3g). The portion of the profile beneath  $1 = Y/D_H$  at the crest shows little change when  $Y$  is reduced from high to medium (Figures 3a and 3g), and the profile merely loses a portion of the free flow above  $2 = Y/D_H$ , until it is lost completely at the low  $Y$  conditions (Figures 3a and 3g). The change in the vertical distribution of shear can explain why the reattachment length increases with  $\bar{U}_c$  at the low flow depths but not at high flow depths, because the gradient of velocity below one dune height at the crest increases once the free flow is lost at the lower depth conditions (Figure 3a). Although form roughness is increased by lowering the flow depth, the effect of very low relative submergence on the shape of the mean velocity profile produces near-bed velocities that are greater for comparable  $\bar{U}_c$  at higher  $Y$ , therefore producing greater skin friction. The threshold for this change appears to be near the classical equilibrium condition, as run M84 produces a similar velocity profile to those at the low flow depth conditions.

The length of flow separation over dunes has previously been shown to vary with hydraulic and geometric conditions, such as dune height and crestal shape (Araújo et al., 2013; Dimas et al., 2008; Engel, 1981; Kwoil et al., 2016; Simpson, 1989), leeside angle (Best & Kostaschuk, 2002; Kwoil et al., 2016), flow depth (Balachandar et al., 2007), flow velocity (Araújo et al., 2013; Engel, 1981), downstream bedform shape and distance (Dimas et al., 2008; Engel, 1981), and crestline curvature (Venditti, 2007). Such an array of controls has resulted in the parametrization of flow separation length tending to be achieved using empirically defined relationships derived from specific data sets, and thus not necessarily providing a fundamental description of the multitude of processes involved (e.g., Lefebvre et al., 2014; Paarlberg et al., 2007). The present results demonstrate that there is a significant behavioral shift in reattachment length without a change in bedform geometry, therefore indicating that relative submergence, which affects the shape of the velocity profiles, is a first-order control. The quantification of reattachment length (Figure 4) indicates that a measure of flow magnitude and the shape of velocity profiles provide a more universal description of reattachment length for a given dune geometry. Parameterization of this relationship into models such as those of Paarlberg et al. (2007) and Lefebvre et al. (2014) will require additional work measuring velocity profiles and median reattachment lengths across a range of dune geometries, including low-angle dunes, as well as considering the inclusion of brink-point shape into dune morphology (Kwoil et al., 2016, 2017).

### 4.3. Implications for the Stability of Dunes

Experiments conducted where bedform morphology, flow depth, and flow velocity were in equilibrium have found that the wake region has a limit of one dune height above the bed (Bennett & Best, 1995; Nelson et al., 1993). The analysis presented herein of turbulent flow over fixed 2-D dunes indicates that changing  $\bar{U}_c$  from incoming flow velocities that are too low to form dunes (e.g., H14, M14 and L18) to velocities near upper-stage plane bed conditions (e.g., H92) has a major impact on the height and location of the largest turbulent intensities in the turbulent wake.

The importance of topographic acceleration has been emphasized in studies on the ripple-dune transition (Bennett & Best, 1996; Fernandez et al., 2006; Robert & Uhlman, 2001; Schindler & Robert, 2005), with the transition from ripples to dunes usually occurring when there is large topographic acceleration along a large *rogue* ripple that produces trough scour through a higher downstream velocity gradient at the crest (Bennett & Best, 1996; Fernandez et al., 2006). These larger trough and wake change the location of turbulent events along the downstream ripple, thus promoting the generation of dunes downstream (Venditti et al., 2005). The low  $\bar{U}_c$  conditions described herein build on this knowledge and indicate why dunes do not form at low flow velocities (e.g., H14) where there is insufficient topographic acceleration to promote larger

troughs through the spatial confinement of (1) the reattachment length, and (2) high intensity turbulent Q2 and Q4 events near the reattachment point.

Topographic acceleration in depth-limited flows produces a notable free surface response that further promotes flow acceleration through flow convergence (McLean, 1990). However, dunes that have been measured in deeper flows ( $>3.5 D_H$ ) often show no free surface response (McLean et al., 1994) that suggests that the influence of topographic acceleration decreases with higher depth (measured as a lower gradient in mean downstream velocity profile). However, a reduction in topographic acceleration produced little change in the magnitude of shear stress over the stoss side (McLean et al., 1994). This result was also noted in the present study where the magnitude of Reynolds stresses scaled only with  $\bar{U}_c$  and not with relative submergence ( $Y/D_H$ ) (Table 1). Importantly, the present study shows that while the magnitude of Reynolds stress scales with  $\bar{U}_c$ , it is the spatial distribution of Reynolds stress—and particularly the significant Q2 and Q4 Reynolds stress events—that changes with  $\bar{U}_c$  and  $Y$  as a result of different topographic forcing. In flows with significant free surface interaction, it is likely that the additional flow acceleration and convergence over the stoss, produced by free surface interaction and deformation through flow convergence, explain why higher  $\bar{U}_c$  conditions are required to produce dunes in deeper flows across equal grain sizes in stability diagrams (Southard & Boguchwal, 1990, their Figure 2). Deeper flows would create less flow convergence from the free surface interaction, therefore moving the turbulent wake and stacked wake toward the free surface, and away from the bed (e.g., H14).

#### 4.4. Implications for Dune Shape

The dune crest is a critical area, as the location and direction of maximum bed shear stress define the type of bedform produced (Yalin, 1977). Using linear stability analysis, McLean (1990) reiterated the importance of a phase lag between flow velocity and sediment flux on the stability of dunes, where the maximum sediment flux is upstream of the crest, thus promoting vertical deposition of sediment as the bedform migrates downstream (Naqshband et al., 2017). Bennett et al. (1998) demonstrated that dunes lose stability and transform into upper-stage plane beds when the location of maximum sediment transport flux moves downstream of the  $\bar{U}_c$  maximum. The dune shape that occurs before the transition is characterized by a long flat crest and deep trough. These dunes are often called *washed-out dunes*, or *humpback dunes* (Bridge & Best, 1988; Carling, Golz, et al., 2000; Engel, 1981; Saunderson & Lockett, 1983), where, under a high  $\bar{U}_c$ , the dune crest possesses upper-stage plane bed conditions. In the present experiments, the mean vertical distribution of momentum at the crest becomes more positive (vertical) with increasing  $\bar{U}_c$  until  $\sim 0.60$  m/s (Table 1), indicating that the interplay between topographic acceleration over the rising stoss slope is dominant over the effects of flow convergence at the crest. Above  $\bar{U}_c = 0.60$  m/s mean flow velocity, the effects of flow convergence start to become more dominant as negative vertical velocities are found in the mean vertical velocity profiles near the free surface (Figure 3j), producing lower  $\bar{V}_c$ . It is interpreted herein that for the fixed geometry of dunes studied, flow conditions above  $\sim 0.60$  m/s gradually move away from equilibrium dune conditions. Yalin (1977) demonstrated that dune height scales with dimensionless bed shear stress up to  $\sim 9 \theta^*/\theta_c^*$  ( $\sim 0.60$  m/s  $\bar{U}_c$  in this study, Table 1), after which dune height lowers with greater dimensionless bed shear stress. The peak in dune height at  $\sim 9 \theta^*/\theta_c^*$  closely matches the conditions at  $\sim 0.60$  m/s  $\bar{U}_c$  (H61 and L62, Table 1). The present data show that a similar relationship occurs with  $\bar{V}_c$  and  $\bar{U}_c$ , which is possibly more indicative of the effects of flow convergence and topographic acceleration that are representative of the pressure field, and provides a first-order control on dune height and shape.

The impact of differing degrees of flow convergence, topographic acceleration, and spatial confinement of Reynolds stress near flow reattachment is illustrated conceptually in Figure 8. It is hypothesized that under mobile bed conditions, humpback dune shapes would likely be present above  $\sim 0.60$  m/s for the grain sizes and conditions used herein ( $> 10 \theta^*/\theta_c^*$ ) due to the extent of flow convergence at the crest and the shape of the velocity profiles at high  $\bar{U}_c$  conditions, where the linear (lower) portion of the mean velocity profile makes up the majority of the velocity profile at the crest (Figures 3g and 3j). Additionally, the progressively larger area of high-frequency quadrant events seen downstream of reattachment (Figures 5 and 6) should produce deeper and longer dune troughs under mobile bed conditions, similar to humpback dunes. It is worthy of note that similar turbulent characteristics and dune shapes have been observed when measuring turbulent flow over dunes that are underneath an ice cover (Smith & Ettema, 1997),

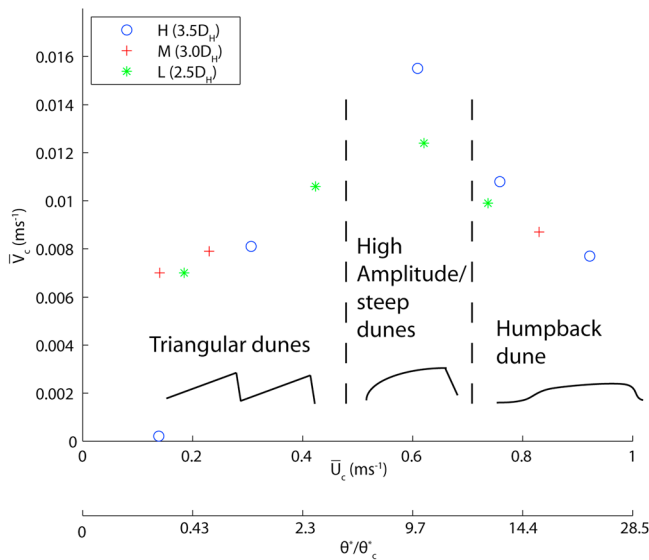


**Figure 8.** The changes in flow structure found in the present experiments plotted alongside common bedform shapes found under comparable mobile bed conditions. At low transport stage ( $\theta^*/\theta_c^*$  up to  $\sim 2$ ) the low topographic acceleration produces triangular bedforms due to minimal crestal flattening and trough scour. At higher transport stage ( $\theta^*/\theta_c^* \sim 8-12$ ) deposition at the crest is promoted by high vertical velocities, while higher Reynolds stresses at reattachment promote trough scour, producing the tallest dunes. Humpback dune shapes form at higher transport stage ( $\theta^*/\theta_c^* > 12$ ) when flow convergence reduces  $\bar{V}_c$ , thus reducing deposition and bedform height and thereby flattening the crest. Dune shapes are adapted from Carling, Golz, et al. (2000, their Figure 5).

( $< 8 \theta^*/\theta_c^*$ ). High-amplitude dunes produce flow acceleration and flow convergence along the stoss slope, which act to increase  $\bar{V}_c$  (Figures 3a and 3g) and thus promote vertical deposition. In combination with the higher Reynolds stresses, the higher  $\bar{U}_c$  operates in tandem to produce the highest amplitude bedforms in the middle of the dune stability field  $\sim 8$  to  $12 \theta^*/\theta_c^*$  (Figure 8) and therefore provides a process-based explanation for the variations in dune shape, and their varying amplitude, with bed shear stress as shown by Yalin (1977).

Alteration in the shape of the velocity profile will also have an impact on the scaling of dune height. Traditionally, equilibrium dune height has been reasoned to scale with flow depth (Fredsoe, 1982; Simons & Richardson, 1962, 1966; Yalin, 1977). However, field surveys have often documented dune fields where the bedform scale is smaller than expected for a given flow depth, particularly in larger river channels (Bradley & Venditti, 2017; Leclair, 2011; Parsons et al., 2005). As Figures 3e and 3k demonstrate, even a relatively small increase in flow depth of  $0.5 D_H$  above the equilibrium flow depth can produce a substantial change in the direction of vertical velocity above the leeside shear layer (Figure 3). This indicates that any suspended bed sediment from the stoss side will likely fall out onto the shear layer at this depth, rather than falling onto the lee or stoss slopes and adding to bedload transport. As relatively rapid depth changes of  $0.5 D_H$  are common in natural rivers (Aberle et al., 2010), this implication, particularly with regard to bedform hysteresis (Martin & Jerolmack, 2013) and its influence on bedload to suspended load ratios, requires further work and exploration.

## 5. Conclusions

Investigation of the two-dimensional flow fields over fixed two-dimensional dune bedforms in nonequilibrium flow-morphology conditions reveals complex relationships between flow depth and velocity, and the location and intensity of turbulence over dunes. The changes in turbulent flow structure in nonequilibrium conditions are summarized in Figure 7 and extend previous conceptual models of flow over

where greater topographic acceleration is produced via suppression of the velocity maximum toward the bed. Topographic acceleration and compression of the free surface also influences the spatial confinement of Reynolds stresses near reattachment, as the distribution of a greater frequency of turbulent events becomes more spatially confined toward flow reattachment for the higher  $Y$  conditions (Figures 5 and 6). This spatial change in turbulent flow structure may also explain the deep troughs seen in humpback dunes (Carling, Golz, et al., 2000; Smith & Ettema, 1997).

As both Nelson et al. (1995) and Engel (1981) report, the wake and flow reattachment downstream of a single backward facing step are longer than over a train of bedforms, due to the additional influence of topographic acceleration produced by the stoss slope. When topographic acceleration is added via the introduction of a downstream bedform, the length of the wake decreased as the rate of decay in turbulence intensity is higher (Nelson et al., 1993). The present results demonstrate these effects of topographic acceleration can also occur *without* a change in bedform geometry and *with* a change in relative submergence and  $\bar{U}_c$ . The stacked wake, which is the turbulent wake from a dune upstream advected over a downstream dune, as seen at the higher depth conditions, was largest at H30 but became less intense and moved progressively upstream with increases in  $\bar{U}_c$ . This change is likely due to an increase in the rate of decay in turbulence intensity due to higher velocity gradients at higher  $\bar{U}_c$  (Figures 3a and 3g). The high elevation of the turbulent wake seen in condition H14 (Figures 5 and 6) is likely to produce the formation of steeper bedforms due to the lack of topographic acceleration flattening the stoss slope (Figure 8), thus reducing the amount of crestal flattening present under higher  $\bar{U}_c$  or shallower conditions

equilibrium dunes (Best, 2005a) to a wider range of nonequilibrium flow conditions. The present results highlight the following.

1. Reattachment length scales with  $\bar{U}_c/u_c^*$ , with  $u_c^*$  calculated using the law of the wall and the entire velocity profile at the crest. The relation  $R_x/D_H = 2.25 \bar{U}_c/u_c^* + -8.36$  provides a powerful tool for prediction of median flow reattachment length using the incoming flow velocity.
2. The depth-averaged vertical velocity at the dune crest ( $\bar{V}_c$ ), which controls rates of deposition or erosion at the dune crest, was found to show a parabolic relationship with the depth-averaged downstream velocity at the crest ( $\bar{U}_c$ ), with the peak in  $\bar{V}_c$  occurring at  $\sim 0.60$  m/s  $\bar{U}_c$  across all depths tested. This corresponds to the peak in bedform aspect ratio found in past work for mobile bed conditions at  $\sim 10 \theta^*/\theta_c^*$  (Table 1, Venditti et al., 2016; Yalin, 1977). Low values of  $\bar{V}_c$  were found at  $< 8 \theta^*/\theta_c^*$  and  $> 12 \theta^*/\theta_c^*$ , further relating the depth-averaged vertical velocity at the crest with transport stage.
3. The spatial location of the turbulent wake was found to vary with flow depth and velocity. When flow velocity was slower and deeper (e.g., H14,  $\theta^*/\theta_c^* < 1$ ) than equilibrium conditions, the wake rose toward the free surface and away from the bed. Conversely, lower flow depths and higher velocities compressed the turbulent wake toward the bed (e.g., L75,  $\theta^*/\theta_c^* > 10$ ). As there was no variation in bed morphology in the present fixed-bed experiments, this variation in the location of the turbulent wake was a product of the rate of flow acceleration and flow convergence along the dune stoss slope. This explains why higher  $\bar{U}_c$  conditions are required to produce dunes in higher flow depths ( $> 3 D_H$ ) with equal grain size, as shown in bedform phase stability diagrams (Southard & Boguchwal, 1990). Deeper flows will possess less flow convergence resulting from the free surface interaction, therefore moving the turbulent wake and stacked wake toward the free surface, and away from the bed, thus resulting in a reduction of transport stage.

#### Acknowledgments

C. A. Unsworth would like to thank the University of Hull for funding his Ph.D. Scholarship. This research was also supported by grant NE/I014101/1 from the UK Natural Environment Research Council (NERC). The laboratory work was undertaken at the Sorby Environmental Fluid Dynamics Laboratory, University of Leeds, UK, and we are grateful to Professor Jeff Peakall for the use of these facilities. We are very thankful for the helpful reviews of Suleyman Naqshband and two anonymous referees. Data are available from the University of Hull online data repository at <https://hydra.hull.ac.uk/resources/hull:16477>.

#### References

- Aberle, J., Nikora, V., Henning, M., Ettmer, B., & Hentschel, B. (2010). Statistical characterization of bed roughness due to bed forms: A field study in the Elbe River at Aken, Germany. *Water Resources Research*, *46*, W03521. <https://doi.org/10.1029/2008WR007406>
- Adrian, R. J. (2005). Twenty years of particle image velocimetry. *Experiments in Fluids*, *39*(2), 159–169. <https://doi.org/10.1007/s00348-005-0991-7>
- Adrian, R. J., & Westerweel, J. (2011). *Particle image velocimetry*. Cambridge, UK: Cambridge University Press.
- Allen, J. R. L. (1968). *Current ripples: Their relation to patterns of water and sediment motion*. Amsterdam: North-Holland Publishing Company.
- Allen, J. R. L. (1978). Computational models for dune time-lag calculations using Stein's rule for dune height. *Sedimentary Geology*, *20*, 165–216. [https://doi.org/10.1016/0037-0738\(78\)90054-4](https://doi.org/10.1016/0037-0738(78)90054-4)
- Allen, J. R. L. (1982). *Sedimentary structures: Their character and physical basis, volume 1, Developments in Sedimentology* (Vol. 30). Amsterdam: Elsevier Science Publishers.
- Amsler, M. L., & Garcia, M. H. (1997). Discussion sand-dune geometry of large rivers during floods. *Journal of Hydraulic Engineering*, 582–584. [https://doi.org/10.1061/\(ASCE\)0733-9429\(1997\)123:6\(582\)](https://doi.org/10.1061/(ASCE)0733-9429(1997)123:6(582))
- Araújo, A. D., Parteli, E. J. R., Pöschel, T., Andrade, J. S., & Herrmann, J. H. (2013). Numerical modelling of the wind flow over a transverse dune. *Scientific Reports*, *3*(1), 2858. <https://doi.org/10.1038/srep02858>
- Baas, J. H., Best, J. L., & Peakall, J. (2011). Depositional processes, bedform development and hybrid bed formation in rapidly decelerated cohesive (mud–sand) sediment flows. *Sedimentology*, *58*(7), 1953–1987. <https://doi.org/10.1111/j.1365-3091.2011.01247.x>
- Baas, J. H., Best, J. L., & Peakall, J. (2016). Predicting bedforms and primary current lamination in cohesive mixtures of mud and sand. *Journal of the Geological Society of London*, *173*(1), 12–45. <https://doi.org/10.1144/jgs2015-024>
- Balachandar, R., Hyun, B. S., & Patel, V. C. (2007). Effect of depth on flow over a fixed dune. *Canadian Journal of Civil Engineering*, *34*(12), 1587–1599. <https://doi.org/10.1139/07-068>
- Bennett, J. L., & Best, J. (1996). Mean flow and turbulence structure over fixed ripples and the ripple dune transition. In P. J. Ashworth, S. J. Bennett, J. L. Best, & S. J. McLelland (Eds.), *Coherent flow structures in open channels* (pp. 281–304). Chichester: Wiley & Sons.
- Bennett, S., & Best, J. (1995). Mean flow and turbulence structure over fixed, two-dimensional dunes: Implications for sediment transport and bedform stability. *Sedimentology*, *42*(3), 491–513. <https://doi.org/10.1111/j.1365-3091.1995.tb00386.x>
- Bennett, S. J., Bridge, J. S., & Best, J. L. (1998). Fluid and sediment dynamics of upper stage plane beds. *Journal of Geophysical Research*, *103*(C1), 1239–1274. <https://doi.org/10.1029/97JC02764>
- Best, J. L. (1992). On the entrainment of sediment and initiation of bed defects: Insights from recent developments within turbulent boundary layer research. *Sedimentology*, *39*(5), 797–811. <https://doi.org/10.1111/j.1365-3091.1992.tb02154.x>
- Best, J. L. (1996). The fluid dynamics of small-scale alluvial bedforms. In P. A. Carling & M. R. Dawson (Eds.), *Advances in Fluvial Dynamics and Stratigraphy* (pp. 67–125). Chichester: John Wiley and Sons.
- Best, J. L. (2005a). The kinematics, topology and significance of dune related macroturbulence: Some observations from the laboratory and field. In M. D. Blum, S. B. Marriott, & S. Leclair (Eds.), *Fluvial Sedimentology VII* (Vol. 35, pp. 41–60). Special Publication of the International Association of Sedimentologists. <https://doi.org/10.1002/9781444304350.ch3>
- Best, J. L. (2005b). The fluid dynamics of river dunes: A review and some future research directions. *Journal of Geophysical Research*, *110*, F04S02. <https://doi.org/10.1029/2004JF000218>
- Best, J., & Kostaschuk, R. (2002). An experimental study of turbulent flow over a low-angle dune. *Journal of Geophysical Research*, *107*(C9), 3135. <https://doi.org/10.1029/2000JC000294>



- Bogard, D. G., & Tiederman, W. G. (1986). Burst detection with single point velocity measurements. *Journal of Fluid Mechanics*, *162*(1), 389–413. <https://doi.org/10.1017/S0022112086002094>
- Bradley, R. W., & Venditti, J. G. (2017). Reevaluating dune scaling relations. *Earth-Science Reviews*, *165*, 356–376. <https://doi.org/10.1016/j.earscirev.2016.11.004>
- Bridge, J. S., & Best, J. L. (1988). Flow, sediment transport and bedform dynamics over the transition from dunes to upper-stage plane beds: Implications for the formation of planar laminae. *Sedimentology*, *35*(5), 753–763. <https://doi.org/10.1111/j.1365-3091.1988.tb01249.x>
- Carling, P. A., Golz, E., Orr, H. G., & Radecki-Pawlik, A. (2000). The morphodynamics of fluvial sand dunes in the River Rhine, near Mainz, Germany. I. Sedimentology and morphology. *Sedimentology*, *47*(1), 227–252. <https://doi.org/10.1046/j.1365-3091.2000.00290.x>
- Carling, P. A., Williams, J. J., Golz, E., & Kelsey, A. D. (2000). The morphodynamics of fluvial sand dunes in the River Rhine, near Mainz, Germany. II. Sedimentology and morphology. *Sedimentology*, *47*(1), 253–278. <https://doi.org/10.1046/j.1365-3091.2000.00291.x>
- Celik, A. O., Diplas, P., & Dancy, C. L. (2013). Instantaneous turbulent forces and impulse on a rough bed: Implications for initiation of bed material movement. *Water Resources Research*, *49*, 2213–2227. <https://doi.org/10.1002/wrcr.20210>
- Chang, K., & Constantinescu, G. (2013). Coherent structures in flow over two-dimensional dunes. *Water Resources Research*, *49*(5), 2446–2460. <https://doi.org/10.1002/wrcr.20239>
- Chen, J., Wang, Z., Li, M., Wei, T., & Chen, Z. (2012). Bedform characteristics during falling flood stage and morphodynamic interpretation of the middle–lower Changjiang (Yangtze) River channel, China. *Geomorphology*, *147–148*, 18–26. <https://doi.org/10.1016/j.geomorph.2011.06.042>
- Dimas, A. A., Fourniotis, N. T., Vouros, A. P., & Demetropoulos, A. P. (2008). Effect of bed dunes on spatial development of open-channel flow. *Journal of Hydraulic Research*, *46*(6), 802–813. <https://doi.org/10.1080/00221686.2008.9521924>
- Diplas, P., Dancy, C. L., Celik, A. O., Valyrakis, M., Greer, K., & Akar, T. (2008). The role of impulse on the initiation of particle movement under turbulent flow conditions. *Science*, *322*(5902), 717–720. <https://doi.org/10.1126/science.1158954>
- Engel, P. (1981). Length of flow separation over dunes. *Journal of Hydraulic Division. American Society of Civil Engineers*, *107*(HY10), 113–1143.
- Fedele, J. J., & Garcia, M. H. (2001). Alluvial roughness in streams with dunes: A boundary-layer approach. In G. Seminara & P. Blondeaux (Eds.), *River, Coastal and Estuarine Morphodynamics* (pp. 37–60). New York: Springer. [https://doi.org/10.1007/978-3-662-04571-8\\_3](https://doi.org/10.1007/978-3-662-04571-8_3)
- Fernandez, R., Best, J., & López, F. (2006). Mean flow, turbulence structure, and bed form superimposition across the ripple-dune transition. *Water Resources Research*, *42*, W054063. <https://doi.org/10.1029/2005WR004330>
- Fredsoe, J. (1982). Shape and dimensions of stationary dunes in rivers. *Journal of the Hydraulics Division of the American Society of Civil Engineers*, *108*, 932–947.
- Frias, C. E., & Abad, J. D. (2013). Mean and turbulent flow structure during the amalgamation process in fluvial bed forms. *Water Resources Research*, *49*, 6548–6560. <https://doi.org/10.1002/wrcr.20456>
- Garcia, M. H., Nino, Y., & Lopez, F. (1996). Laboratory observations of particle entrainment into suspension by turbulent bursting. In P. J. Ashworth, S. J. Bennett, J. L. Best, & S. J. McLelland (Eds.), *Coherent Flow Structures in Open Channels* (pp. 285–319). Chichester: Wiley & Sons.
- Grass, J. (1983). The influence of boundary layer turbulence on the mechanics of sediment transport. In M. Sumer & A. B. Muller (Eds.), *Proceedings of Euromech 156, Mechanics of Sediment Transport, Istanbul* (pp. 3–18). Rotterdam: A.A.Balkema.
- Grigoriadis, D. G. E., Balaras, E., & Dimas, A. A. (2009). Large-eddy simulations of unidirectional water flow over dunes. *Journal of Geophysical Research*, *114*, F02022. <https://doi.org/10.1029/2008JF001014>
- Guy, H. P., Simons, D. B., & Richardson, E. V. (1966). Summary of alluvial channel data from flume experiments 1956–61. U.S. Geological Survey Professional Paper 462-I, Department of the Interior, Washington, DC.
- Hardy, R. J., Lane, S. N., Lawless, M. R., Best, J. L., Elliott, L., & Ingham, D. B. (2005). Development and testing of a numerical code for treatment of complex river channel topography in three-dimensional CFD models with structured grids. *Journal of Hydraulic Research*, *43*(5), 468–480. <https://doi.org/10.1080/00221680509500145>
- Jordan, B. P. R. (1965). Fluvial sediment of the Mississippi River at St. Louis, Missouri. Geological Survey Water-Supply Paper 1802. U.S. Department of the Interior, Washington, DC.
- Julien, P. Y., & Klasssen, G. J. (1995). Sand-dune geometry of large river during floods. *Journal of Hydraulic Engineering*, *121*(9), 657–633. [https://doi.org/10.1061/\(ASCE\)0733-9429\(1995\)121:9\(657](https://doi.org/10.1061/(ASCE)0733-9429(1995)121:9(657)
- Kadota, A., & Nezu, I. (1999). Three-dimensional structure of space-time correlation on coherent vortices generated behind dune crest. *Journal of Hydraulic Research*, *37*(1), 59–80. <https://doi.org/10.1080/00221689909498532>
- Kostaschuk, R., & Church, M. A. (1993). Macroturbulence generated by dunes: Fraser River, Canada. *Sedimentary Geology*, *85*(1–4), 25–37. [https://doi.org/10.1016/0037-0738\(93\)90073-E](https://doi.org/10.1016/0037-0738(93)90073-E)
- Kwoll, E., Venditti, J. G., Bradley, R. W., & Winter, C. (2016). Flow structure and resistance over subaqueous high- and low-angle dunes. *Journal of Geophysical Research: Earth Surface*, *121*, 545–564. <https://doi.org/10.1002/2015JF003637>
- Kwoll, E., Venditti, J. G., Bradley, R. W., & Winter, C. (2017). Observations of coherent flow structures over subaqueous high- and low-angle dunes. *Journal of Geophysical Research: Earth Surface*, *122*, 2244–2268. <https://doi.org/10.1002/2017JF004356>
- Lapointe, M. F. (1992). Burst-like sediment suspension events in a sand bed river. *Earth Surface Processes and Landforms*, *17*(3), 253–270. <https://doi.org/10.1002/esp.3290170305>
- Lapointe, M. F. (1996). Frequency spectra and intermittency of the turbulent suspension process in a sand-bed river. *Sedimentology*, *43*(3), 439–449. <https://doi.org/10.1046/j.1365-3091.1996.d01-18.x>
- Leclair, S. F. (2011). Interpreting fluvial hydromorphology from the rock record: Large-river peak flows leave no clear signature. In C. Davidson, S. K. Leleu, & S. North (Eds.), *River to Rock Record: the Preservation of Fluvial Sediments and their Subsequent Interpretation* (pp. 112–124). SEPM Special Publication.
- Lefebvre, A., Paarlberg, A. J., & Winter, C. (2014). Flow separation and shear stress over angle-of-repose bed forms: A numerical investigation. *Water Resources Research*, *50*, 986–1005. <https://doi.org/10.1002/2013WR014587>
- Lefebvre, A., Paarlberg, A. J., & Winter, C. (2016). Characterising natural bedform morphology and its influence on flow. *Geo-Marine Letters*, *36*(5), 379–393. <https://doi.org/10.1007/s00367-016-0455-5>
- Lin, C. Y. M., & Venditti, J. G. (2013). An empirical model of subcritical bedform migration. *Sedimentology*, *60*(7), 1786–1799. <https://doi.org/10.1111/sed.12056>
- Lu, S. S., & Willmarth, W. W. (1973). Measurements of the structure of the Reynolds stress in a turbulent boundary layer. *Journal of Fluid Mechanics*, *60*(3), 481–511. <https://doi.org/10.1017/S0022112073000315>
- Maddux, T. B., Mclean, S. R., & Nelson, J. M. (2003). Turbulent flow over three-dimensional dunes: 2. Fluid and bed stresses. *Journal of Geophysical Research*, *108*(F1), 6010. <https://doi.org/10.1029/2003JF000018>
- Martin, R. L., & Jerolmack, D. J. (2013). Origin of hysteresis in bed form response to unsteady flows. *Water Resources Research*, *49*, 1314–1333. <https://doi.org/10.1002/wrcr.20093>

- Mazumder, B., Pal, D., Ghoshal, K., & Ojha, S. (2009). Turbulence statistics of flow over isolated scalene and isosceles triangular-shaped bedforms. *Journal of Hydraulic Research*, 47(5), 626–637. <https://doi.org/10.3826/jhr.2009.3397>
- McLean, S. R. (1990). The stability of ripples and dunes. *Earth Science Reviews*, 29(1-4), 131–144. [https://doi.org/10.1016/0012-8252\(90\)90032-Q](https://doi.org/10.1016/0012-8252(90)90032-Q)
- McLean, S. R., Nelson, J., & Wolfe, S. R. (1994). Turbulence structure over two-dimensional bed forms implications for sediment transport. *Journal of Geophysical Research*, 99(C6), 12,729–12,747. <https://doi.org/10.1029/94JC00571>
- McLean, S. R., Wolfe, S. R., & Nelson, J. M. (1999). Spatially averaged flow over a wavy boundary revisited. *Journal of Geophysical Research*, 104(C7), 15,743–15,753. <https://doi.org/10.1029/1999JC900116>
- Naqshband, S., Hoitink, A. J. F., McElroy, B., Hurther, D., & Hulscher, S. J. M. H. (2017). A sharp view on river dune transition to upper stage plane bed. *Geophysical Research Letters*, 44, 11,437–11,444. <https://doi.org/10.1002/2017GL075906>
- Naqshband, S., van Duin, O., Ribberink, J., & Hulscher, S. (2016). Modeling river dune development and dune transition to upper stage plane bed. *Earth Surface Processes and Landforms*, 41(3), 323–335. <https://doi.org/10.1002/esp.3789>
- Nelson, J. M., Logan, B. L., Kinzel, P. J., Shimizu, Y., Giri, S., Shreve, R. L., et al. (2011). Bedform response to flow variability. *Earth Surface Processes and Landforms*, 36(14), 1938–1947. <https://doi.org/10.1002/esp.2212>
- Nelson, J. M., McLean, S. R., & Wolfe, S. R. (1993). Mean flow and turbulence fields over two dimensional bed forms. *Water Resources Research*, 29(12), 3935–3953. <https://doi.org/10.1029/93WR01932>
- Nelson, J. M., Shreve, R. L., McLean, S. R., & Drake, T. G. (1995). Role of near-bed turbulence structure in bed load transport and bed form mechanics. *Water Resources Research*, 31(8), 2071–2086. <https://doi.org/10.1029/95WR00976>
- Nelson, J. M., & Smith, J. D. (1989). Mechanics of flow over ripples and dunes. *Journal of Geophysical Research*, 94(C6), 8146–8162. <https://doi.org/10.1029/JC094iC06p08146>
- Nicholas, A. P., Ashworth, P. J., Sambrook-Smith, G. H., & Sandbach, S. D. (2013). Numerical simulation of bar and island morphodynamics in anabranching mega rivers. *Journal of Geophysical Research: Earth Surface*, 118, 2019–2044. <https://doi.org/10.1002/jgrf.20132>
- Nino, Y., Lopez, F., & Garcia, M. (2003). Threshold for particle entrainment into suspension. *Sedimentology*, 50(2), 247–263. <https://doi.org/10.1046/j.1365-3091.2003.00551.x>
- Nittrouer, J. A., Allison, M. A., & Campanella, R. (2008). Bedform transport rates for the lowermost Mississippi River. *Journal of Geophysical Research*, 113, F03004. <https://doi.org/10.1029/2007JF000795>
- Omidyeganeh, M., & Piomelli, U. (2011). Large-eddy simulation of two-dimensional dunes in a steady, unidirectional flow. *Journal of Turbulence*, 12(42), 1–31. <https://doi.org/10.1080/14685248.2011.609820>
- Omidyeganeh, M. H., & Piomelli, U. (2013a). Large-eddy simulation of three-dimensional dunes in a steady, unidirectional flow. Part 1. Turbulence statistics. *Journal of Fluid Mechanics*, 721, 454–483. <https://doi.org/10.1017/jfm.2013.36>
- Omidyeganeh, M. H., & Piomelli, U. (2013b). Large-eddy simulation of three-dimensional dunes in a steady, unidirectional flow. Part 2. Flow structures. *Journal of Fluid Mechanics*, 734, 509–534. <https://doi.org/10.1017/jfm.2013.499>
- Omidyeganeh, M. H., Piomelli, U., Christensen, K. T., & Best, J. L. (2013). Large eddy simulation of interacting barchan dunes in a steady, unidirectional flow. *Journal of Geophysical Research: Earth Surface*, 118, 2089–2104. <https://doi.org/10.1002/jgrf.20149>
- Paarlberg, A. J., Dohmen-Janssen, C. M., Hulscher, S. J. M. H., & Termes, P. (2007). A parameterization of flow separation over subaqueous dunes. *Water Resources Research*, 43, W12417. <https://doi.org/10.1029/2006WR005425>
- Paarlberg, A. J., Dohmen-Janssen, C. M., Hulscher, S. J. M. H., Termes, P., & Schielen, R. (2010). Modelling the effect of time-dependent river dune evolution on bed roughness and stage. *Earth Surface Processes and Landforms*, 35(15), 1854–1866. <https://doi.org/10.1002/esp.2074>
- Parsons, D. R., Best, J. L., Orfeo, O., Hardy, R. J., Kostaschuk, R., & Lane, S. N. (2005). Morphology and flow fields of three-dimensional dunes, Rio Parana Argentina: Results from simultaneous multibeam echo sounding and acoustic Doppler current profiling. *Journal of Geophysical Research*, 110, F04S03. <https://doi.org/10.1029/2004JF000231>
- Prent, T.H., Hickin, E.J. (2001). Annual regime of bedforms, roughness and flow resistance, Lillooet River, British Columbia, BC. [https://doi.org/10.1016/S0169-555X\(01\)00068-X](https://doi.org/10.1016/S0169-555X(01)00068-X)
- Rhoads, B. L., Sukhodolov, N., Fisheries, I., & Rhoads, B. L. (2001). Field investigation of three-dimensional flow structure. *Water Resources Research*, 37(9), 2411–2424. <https://doi.org/10.1029/2001WR000316>
- Robert, A., & Uhlman, W. (2001). An experimental study on the ripple dune transition. *Earth Surface Processes and Landforms*, 26(6), 615–629. <https://doi.org/10.1002/esp.211>
- Saunders, H. C., & Lockett, F. P. J. (1983). Flume experiments on bedforms and structures at the dune-bed transition. In J. D. Collinson & J. Lewin (Eds.), *Modern and ancient fluvial systems* (pp. 48–58). Oxford, UK: Blackwell Publishing Ltd. <https://doi.org/10.1002/9781444303773.ch4>
- Schindler, R. J., & Robert, A. (2005). Flow and turbulence structure across the ripple-dune transition: An experiment under mobile bed conditions. *Sedimentology*, 52(3), 627–649. <https://doi.org/10.1111/j.1365-3091.2005.00706.x>
- Schmeeckle, M. W. (2014). Numerical simulation of turbulence and sediment transport of medium sand. *Journal of Geophysical Research: Earth Surface*, 119, 1240–1262. <https://doi.org/10.1002/2013JF002911>
- Schmeeckle, M. W., Nelson, J. M., & Shreve, R. L. (2007). Forces on stationary particles in near-bed turbulent flows. *Journal of Geophysical Research*, 112, F02003. <https://doi.org/10.1029/2006JF000536>
- Shimizu, Y., Giri, S., Yamaguchi, S., & Nelson, J. (2009). Numerical simulation of dune-flat bed transition and stage-discharge relationship with hysteresis effect. *Water Resources Research*, 45, W04429. <https://doi.org/10.1029/2008WR006830>
- Simons, D. B., & Richardson, E. V. (1962). The effect of bed roughness on depth-discharge relations in alluvial channels. Geological Survey Professional Paper 1498-E, U.S. Department of the Interior, Washington, DC.
- Simons, D. B., & Richardson, E. V. (1966). The effect of bed roughness on depth- discharge relations in alluvial channels. Geological Survey Water-Supply Paper 1498-E
- Simpson, R. L. (1989). Turbulent boundary-layer separation. *Annual Review of Fluid Mechanics*, 21(1), 205–232. <https://doi.org/10.1146/annurev.fl.21.010189.001225>
- Simpson, R. L. (1996). Aspects of turbulent boundary-layer separation. *Progress in Aerospace Science*, 32(5), 457–521. [https://doi.org/10.1016/0376-0421\(95\)00012-7](https://doi.org/10.1016/0376-0421(95)00012-7)
- Smith, B. T., & Ettema, R. (1997). Ice-cover influence on flow structure over dunes ice-cover influence on flow structure over dunes. *Journal of Hydraulic Research*, 35(5), 707–720. <https://doi.org/10.1080/00221689709498403>
- Soulsby, R. (1997). *Dynamics of marine sands*. London, UK: Thomas Telford Publications.
- Southard, J. B., & Boguchwal, L. A. (1990). Bed configurations in steady unidirectional water flows. Part 2. Synthesis of flume data. *Journal of Sedimentary Petrology*, 60(5), 658–679. <https://doi.org/10.1306/212F9241-2B24-11D7-8648000102C1865D>

- Stoesser, T., Braun, C., García-Villalba, M., & Rodi, W. (2008). Turbulence Structures in Flow over Two-Dimensional Dunes. *Journal of Hydraulic Engineering*, 134(1), 42–55. [https://doi.org/10.1061/\(ASCE\)0733-9429\(2008\)134:1\(42\)](https://doi.org/10.1061/(ASCE)0733-9429(2008)134:1(42))
- Theunissen, R., Scarano, F., & Riethmuller, M. L. (2010). Spatially adaptive PIV interrogation based on data ensemble. *Experiments in Fluids*, 48(5), 875–887. <https://doi.org/10.1007/s00348-009-0782-7>
- Van den Berg, J. H., & Van Gelder, A. (1993). A new bedform stability diagram, with emphasis on the transition of ripples to plane bed in flows over fine sand and silt. *Special Publication of the International Association of Sedimentologists*, 17, 11–21.
- Van Rijn, L. C. (1984). Sediment transport Part III Bed forms and alluvial roughness. *Journal of Hydraulic Engineering*, 110(10), 1733–1754.
- Venditti, J. (2007). Turbulent flow and drag over fixed two and three-dimensional dunes. *Journal of Geophysical Research*, 112, F04008. <https://doi.org/10.1029/2006JF000650>
- Venditti, J. G., Church, M., & Bennett, S. J. (2005). Bed form initiation from a flat sand bed. *Journal of Geophysical Research*, 110, F01009. <https://doi.org/10.1029/2004JF000149>
- Venditti, J. G., Lin, C.-Y. M., & Kazemi, M. (2016). Variability in bedform morphology and kinematics with transport stage. *Sedimentology*, 63(4), 1017–1040. <https://doi.org/10.1111/sed.12247>
- Westerweel, J., & Scarano, F. (2005). Universal outlier detection for PIV data. *Experiments in Fluids*, 39(6), 1096–1100. <https://doi.org/10.1007/s00348-005-0016-6>
- Wilbers, A. W. E. (2004). *The development and hydraulic roughness of subaqueous dunes*. Netherlands: University of Utrecht.
- Wilbers, A. W. E., & Ten Brinke, W. B. M. (2003). The response of subaqueous dunes to floods in sand and gravel bed reaches of the Dutch Rhine. *Sedimentology*, 50(6), 1013–1034. <https://doi.org/10.1046/j.1365-3091.2003.00585.x>
- Williams, G. P. (1970). Flume width and water depth effects in sediment-transport experiments. Geological Survey Professional Paper 562-H, U.S. Department of the Interior. Washington, DC.
- Wren, D. G., Kuhnle, R. A., & Wilson, C. G. (2007). Measurements of the relationship between turbulence and sediment in suspension over mobile sand dunes in a laboratory flume. *Journal of Geophysical Research*, 112, F03009. <https://doi.org/10.1029/2006JF000683>
- Xie, Z., Lin, B., & Falconer, R. A. (2014). Turbulence characteristics in free-surface flow over two-dimensional dunes. *Journal of Hydro-Environment Research*, 8(3), 200–209. <https://doi.org/10.1016/j.jher.2014.01.002>
- Yalin, M. S. (1964). Geometrical properties of sand waves. *Journal of Hydraulic Division. American Society of Civil Engineers ASCE*, 90, 105–119.
- Yalin, M. S. (1977). *Mechanics of sediment transport* (2nd ed.). Oxford, New York: Pergamon Press.